



Optical, Near-IR, and Sub-mm IFU Observations of the Nearby Dual Active Galactic Nuclei MRK 463

Ezequiel Treister¹ , George C. Privon¹ , Lia F. Sartori², Neil Nagar³, Franz E. Bauer^{1,4,5} , Kevin Schawinski² , Hugo Messias^{6,7} , Claudio Ricci^{1,8,9} , Vivian U^{10,18} , Caitlin Casey¹¹ , Julia M. Comerford¹², Francisco Muller-Sanchez¹², Aaron S. Evans^{13,14}, Carolina Finlez³, Michael Koss^{2,15} , David B. Sanders¹⁶ , and C. Megan Urry¹⁷

¹ Instituto de Astrofísica and Centro de Astroingeniería, Facultad de Física, Pontificia Universidad Católica de Chile, Casilla 306, Santiago 22, Chile; etreiste@astro.puc.cl

² Institute for Astronomy, ETH Zürich, Wolfgang-Pauli-Straße 27, CH-8093 Zurich, Switzerland

³ Universidad de Concepción, Departamento de Astronomía, Casilla 160-C, Concepción, Chile

⁴ Millennium Institute of Astrophysics (MAS), Nuncio Monseñor Sótero Sanz 100, Providencia, Santiago, Chile

⁵ Space Science Institute, 4750 Walnut Street, Suite 205, Boulder, CO 80301, USA

⁶ Joint ALMA Observatory, Alonso de Córdova 3107, Vitacura 763-0355, Santiago, Chile

⁷ European Southern Observatory, Alonso de Córdova 3107, Vitacura, Casilla 19001, 19 Santiago, Chile

⁸ Kavli Institute for Astronomy and Astrophysics, Peking University, Beijing 100871, People's Republic of China

⁹ Chinese Academy of Sciences South America Center for Astronomy and China-Chile Joint Center for Astronomy, Camino El Observatorio 1515, Las Condes, Santiago, Chile

¹⁰ Department of Physics and Astronomy, University of California, Riverside, 900 University Avenue, Riverside, CA 92521, USA

¹¹ Department of Astronomy, The University of Texas at Austin, 2515 Speedway Boulevard Stop C1400, Austin, TX 78712, USA

¹² Department of Astrophysical and Planetary Sciences, University of Colorado Boulder, Boulder, CO 80309, USA

¹³ National Radio Astronomy Observatory, 520 Edgemont Road, Charlottesville, VA 22903, USA

¹⁴ Department of Astronomy, 530 McCormick Road, University of Virginia, Charlottesville, VA 22904, USA

¹⁵ Eureka Scientific Inc., 2452 Delmer St. Suite 100, Oakland, CA 94602, USA

¹⁶ Institute for Astronomy, 2680 Woodlawn Drive, University of Hawaii, Honolulu, HI 96822, USA

¹⁷ Yale Center for Astronomy & Astrophysics, Physics Department, New Haven, CT 06520, USA

Received 2017 August 19; revised 2018 January 17; accepted 2018 January 17; published 2018 February 15

Abstract

We present optical and near-IR Integral Field Unit (IFU) and ALMA band 6 observations of the nearby dual active galactic nuclei (AGNs) Mrk 463. At a distance of 210 Mpc, and a nuclear separation of ~ 4 kpc, Mrk 463 is an excellent laboratory to study the gas dynamics, star formation processes and supermassive black hole (SMBH) accretion in a late-stage gas-rich major galaxy merger. The IFU observations reveal a complex morphology, including tidal tails, star-forming clumps, and emission-line regions. The optical data, which map the full extent of the merger, show evidence for a biconical outflow and material outflowing at >600 km s⁻¹, both associated with the Mrk 463E nucleus, along with large-scale gradients likely related to the ongoing galaxy merger. We further find an emission-line region ~ 11 kpc south of Mrk 463E that is consistent with photoionization by an AGN. Compared to the current AGN luminosity, the energy budget of the cloud implies a luminosity drop in Mrk 463E by a factor of 3–20 over the last 40,000 years. The ALMA observations of ¹²CO(2–1) and adjacent 1 mm continuum reveal the presence of $\sim 10^9 M_{\odot}$ in molecular gas in the system. The molecular gas shows velocity gradients of ~ 800 km s⁻¹ and ~ 400 km s⁻¹ around the Mrk 463E and 463W nuclei, respectively. We conclude that, in this system, the infall of $\sim 100s M_{\odot} \text{ yr}^{-1}$ of molecular gas is in rough balance with the removal of ionized gas by a biconical outflow being fueled by a relatively small, $<0.01\%$ of accretion onto each SMBH.

Key words: galaxies: active – galaxies: individual (Mrk 463) – galaxies: interactions – galaxies: Seyfert

1. Introduction

For the last ~ 30 years, there has been growing evidence for a strong connection between major, $<3:1$ mass ratio, galaxy mergers and simultaneous episodes of strong star formation and significant central supermassive black hole (SMBH) growth (e.g., Sanders et al. 1988; Barnes & Hernquist 1991; Di Matteo et al. 2005). Early observations of nearby galaxies carried out with the *Infrared Astronomical Satellite* (IRAS) have shown that the most luminous IR sources appear to be associated with interacting galaxies, as evidenced by the presence of tidal tails,

disrupted morphologies, and other features (Soifer et al. 1984). Theoretical models and computational simulations (e.g., Barnes & Hernquist 1991; Mihos & Hernquist 1996; Springel et al. 2005) have shown that a major galaxy merger provides a very efficient mechanism to drive gas to the nuclear regions of the resulting system, which can in turn fuel the observed star formation bursts and SMBH growth. As a consequence, it is natural to expect that major mergers can play a fundamental role in galaxy evolution (e.g., Hopkins et al. 2006).

Major galaxy mergers can also explain the observed correlations between the mass of the central SMBH and physical properties of its host galaxy (e.g., Di Matteo et al. 2005, 2008). However, so-called “feedback effects” are a key element in setting up this physical connection. Such effects are regularly invoked by semi-analytical models in order to reproduce even basic galaxy properties, such as the luminosity function (e.g., Kauffmann & Charlot 1998, and

¹⁸ University of California Chancellor’s Postdoctoral Fellow.

many others since), as they provide additional sources of energy required to prevent runaway star formation episodes (Benson et al. 2003; Croton et al. 2006; Schawinski et al. 2006). In particular, nuclear activity can play a critical role in the regulation of star formation, as observed in some nearby galaxies (e.g., Alatalo et al. 2015).

Treister et al. (2012) found that, while most active galactic nucleus (AGN) activity is triggered by internal, secular processes and minor galaxy mergers, major mergers are directly linked to the most luminous AGN—quasars—and therefore are responsible for most ($\sim 60\%$) of the SMBH accretion across the cosmic history. A natural consequence of this scenario is that dual AGN—i.e., systems in which the two nuclear SMBHs are growing simultaneously at separations of < 10 kpc—should be relatively common (e.g., Volonteri et al. 2003; Fu et al. 2011a; Van Wassenhove et al. 2012). This particular stage in a major galaxy merger, albeit short—i.e., \sim hundreds Myears (Van Wassenhove et al. 2012; Blecha et al. 2013)—is very relevant for galaxy evolution. As shown by Koss et al. (2012), both the fraction of dual AGN and their individual X-ray luminosities peak at nuclear separations < 10 kpc. This implies that significant and rapid SMBH growth can be directly associated with the dual AGN phase, which in turn might be associated with strong feedback effects on the interstellar medium (e.g., Rupke & Veilleux 2011; Veilleux et al. 2013).

Furthermore, the relative frequency of dual systems can be used to constrain the AGN duty cycle in merger-triggered events. In a rather extreme scenario, if the lifetime of the AGN/quasar phase is similar to the merger timescale, we should expect every merger-triggered system to host a dual AGN. However, the observed fraction of dual AGN is significantly lower, $\sim 2\%$ (Liu et al. 2011; Shen et al. 2011). This can be explained at least in part by the difficulty of detecting and observationally confirming these dual AGN. Confirming the dual AGN nature, even for nearby sources, often requires high spatial resolution radio, near-IR, and/or X-ray observations (e.g., Fu et al. 2011b; Koss et al. 2012; McGurk et al. 2015; Müller-Sánchez et al. 2016). Furthermore, in many cases, the nuclear regions in these systems are subject to large amounts of obscuration (Hopkins et al. 2005; Ricci et al. 2017; Scoville et al. 2017), making their detections even more challenging. Nonetheless, many merger systems lack dual nuclei despite adequate data. This suggests that the AGN duty cycle is shorter than the merger timescale.

In order to study the physical properties of the ionized, atomic, and molecular gas, as well as the dust in confirmed dual AGN in the local universe, $z < 0.1$, we started the Multi-wavelength Observations of Dual AGN (MODA) program.¹⁹ The aim of MODA is to study the growth and co-evolution of galaxies and their SMBHs during merger events, particularly at the later merger stages when feedback and nuclear activity likely peak. MODA currently focuses on 17 confirmed dual AGN distributed across the sky. Our program combines: (i) Atacama Large Millimeter Array (ALMA) observations of molecular gas tracers and dust continuum mm/sub-mm emission; (ii) Very Large Telescope (VLT)/Spectrograph for INtegral Field Observations in the Near Infrared (SINFONI) and Keck/OSIRIS (OH-Suppressing Infra-Red Imaging Spectrograph) maps of H_2 , Pa α , Br γ , [Si VI], and other near-

IR emission lines; and (iii) VLT Multi Unit Spectroscopic Explorer (MUSE) optical Integral Field Unit (IFU) spectroscopic observations, aimed primarily to map the atomic emission lines of H α , H β , [O III], and other atomic species, together with Na D in absorption, in order to measure gas and stellar kinematics, as well as to constrain stellar populations and star formation histories. In addition, we are now in the process of adding mid-IR observations from the VLT spectrometer and imager for the mid-infrared (VISIR) and SOFIA (Stratospheric Observatory for Infrared Astronomy) to study the properties of the hot, ~ 300 – 1000 K, dust in these systems, compute accurate nuclear mid-IR to X-ray flux ratios, and obtain accurate estimates of the bolometric luminosities of each AGN.

Here, we focus on one of the sources in the MODA sample, Mrk 463, for which we recently finished obtaining multi-wavelength IFU observations. Mrk 463 is a nearby, $z = 0.0504$ (Falco et al. 1999) or $d \simeq 210$ Mpc, Ultra-Luminous Infrared Galaxy (ULIRG; Sanders & Mirabel 1996). It was classified as a dual AGN based on *Chandra* X-ray observations reported by Bianchi et al. (2008). The two nuclei are separated by $3''.8 \pm 0''.01$, which roughly corresponds to 3.8 kpc. The *Chandra* observations reveal that both nuclei, Mrk 463E and Mrk 463W, respectively, have relatively low X-ray luminosities of $L_X = 1.5 \times 10^{43}$ erg s $^{-1}$ and 3.8×10^{42} erg s $^{-1}$ in the 2–10 keV band and are heavily obscured, with $N_H = 7.1 \times 10^{23}$ cm $^{-2}$ and 3.2×10^{23} cm $^{-2}$. The AGN nature of the eastern nucleus was independently established by Spitzer spectroscopic observations, as presented by Farrah et al. (2007). Given its distance, nuclear separation, infrared luminosity, and existing multi-wavelength observations, Mrk 463 joins NGC6240 (Komossa et al. 2003), Mrk 739 (Koss et al. 2011) and Mrk 266 (Mazzarella et al. 2012) as prime targets for understanding how SMBHs gain mass and how black hole growth can impact their host galaxies in the dual AGN phase of a major galaxy merger.

In this paper, we present optical and near-IR IFU observations of the nearby dual AGN Mrk 463, obtained with the VLT MUSE and SINFONI, as well as ALMA Cycle 2 observations of $^{12}\text{CO}(2-1)$ and adjacent sub-mm continuum in this system. The main goal is to study the morphology and kinematics of the gas in all its phases using atomic and molecular emission lines as tracers, in order to understand the behavior of the gas that is simultaneously feeding the SMBH and fueling star formation during a major galaxy merger. In Section 2, we describe all the different data sets and data reduction strategies used. In Section 3, we describe the multi-wavelength morphological properties of this system, while in Section 4 we focus on the kinematics. The discussion and conclusions are presented in Sections 5 and 6, respectively. Throughout this paper, we assume a Λ CDM cosmology with $h_0 = 0.7$, $\Omega_m = 0.27$ and $\Omega_\Lambda = 0.73$ (Hinshaw et al. 2009).

2. Data

2.1. MUSE

MUSE is a state-of-the-art, second-generation VLT IFU instrument (Bacon et al. 2010). Its relatively large field of view, ~ 1 arcmin 2 , and broad wavelength coverage, ~ 4800 – 9300 Å, are particularly well-suited to observing the entire physical extents of low-redshift systems (e.g., physical sizes of tens of kpc in a single pointing) across a large spectral range

¹⁹ <http://moda.astro.puc.cl/>

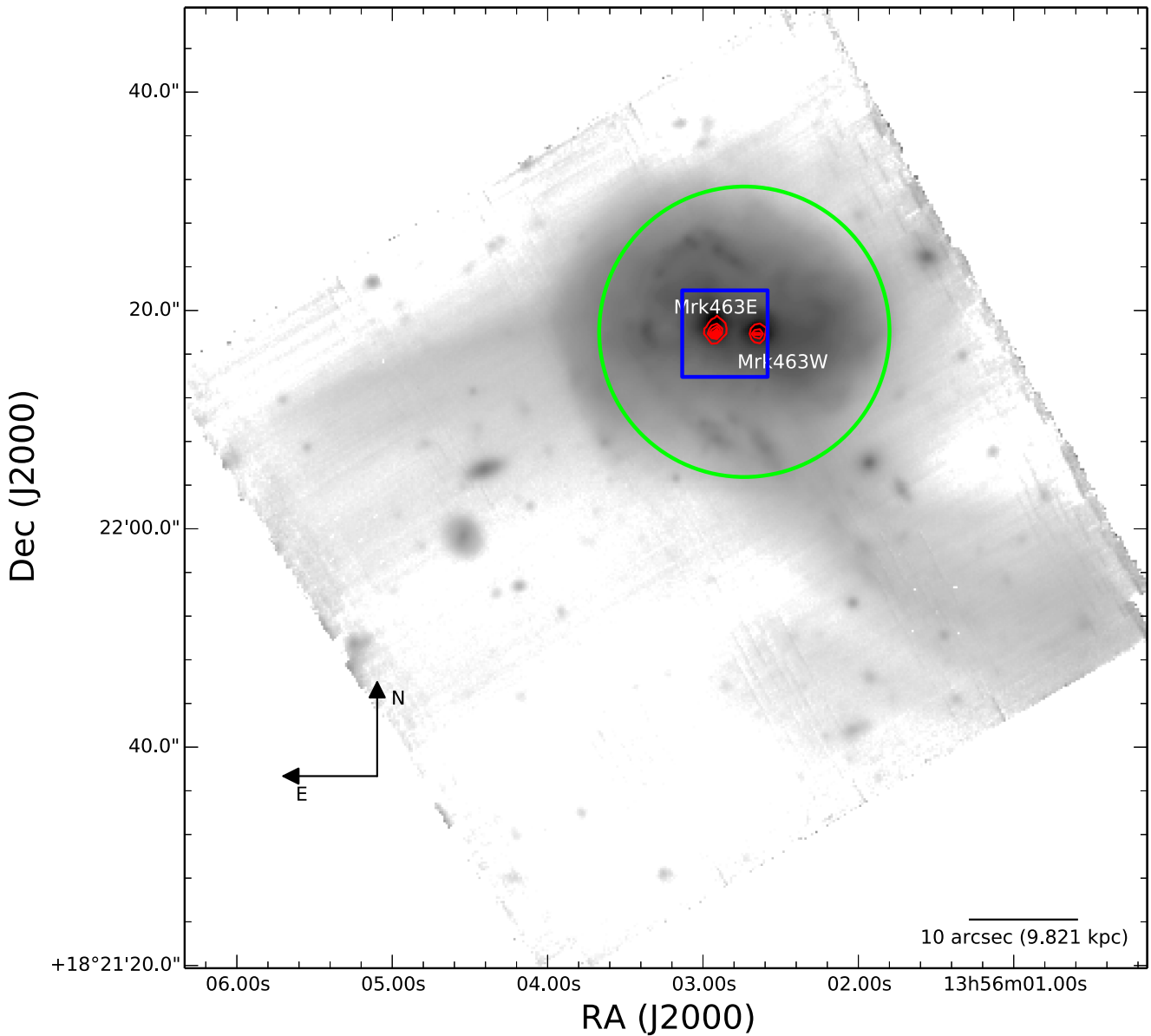


Figure 1. Reconstructed white filter VLT/MUSE image for Mrk 463 covering the entire wavelength range from ~ 4800 to ~ 9300 Å. North is up and east to the left. Pixel scale is the natural $0''.2/\text{pixel}$. Spatial resolution is seeing limited and $\sim 0''.7$. Red contours show the *Chandra* hard X-ray, 2–8 keV, emission while the green circle and blue rectangle highlight the regions covered by the ALMA and VLT/SINFONI observations, respectively.

(simultaneous coverage of the H_β , H_α and [O III] lines, among others). The resolving power of MUSE ranges from 1770 at 4800 Å to 3590 at 9300 Å, which corresponds to velocity resolutions of ~ 80 to ~ 170 km s^{-1} .

Mrk 463 was observed by the VLT/MUSE as part of program 095.B-0482 (PI: E. Treister). Four other nearby dual AGN were also observed as part of this program and will be presented on subsequent papers. Mrk 463 was observed on 2015 July 18 in two 58 min observation blocks (OBs), IDs 1182834 and 1182837, each comprised of three on-target integrations of 976 s plus overheads. Sky conditions were clear, with $< 50\%$ lunar illumination, and a reported ambient seeing $< 0''.8$. The final combined, processed, and calibrated VLT/MUSE data cube for Mrk 463 has an effective exposure time of 5856 seconds (~ 1.6 hours), an average airmass of ~ 1.5 , and an average FWHM of $\sim 0''.7$ based on measurements of stars in the field on the reconstructed white filter image.

Data reduction was carried out using the ESO MUSE pipeline version 1.6.2²⁰ (Weilbacher et al. 2014) in the ESO *Reflex* graphical environment (Freudling et al. 2013). The data reduction stages are standard and include bias and dark current subtraction, flat fielding, wavelength and flux calibration, and astrometric correction. Sky background was subtracted using emission-free regions of the resulting data cube. However, the process is complicated by the large data volume. The MUSE $1' \times 1'$ field of view has 300×300 spatial bins (spaxels) and 4000 spectral bins, such that an individual MUSE frame is a few GB in size and data reduction requires several GB for intermediate products and multiple CPU cores to run. First-look visualizations of the resulting combined data cube were done using the QFitsview²¹ software, but not used in our subsequent

²⁰ Available at <https://www.eso.org/sci/software/pipelines/muse/>.

²¹ <http://www.mpe.mpg.de/~ott/QFitsView/>

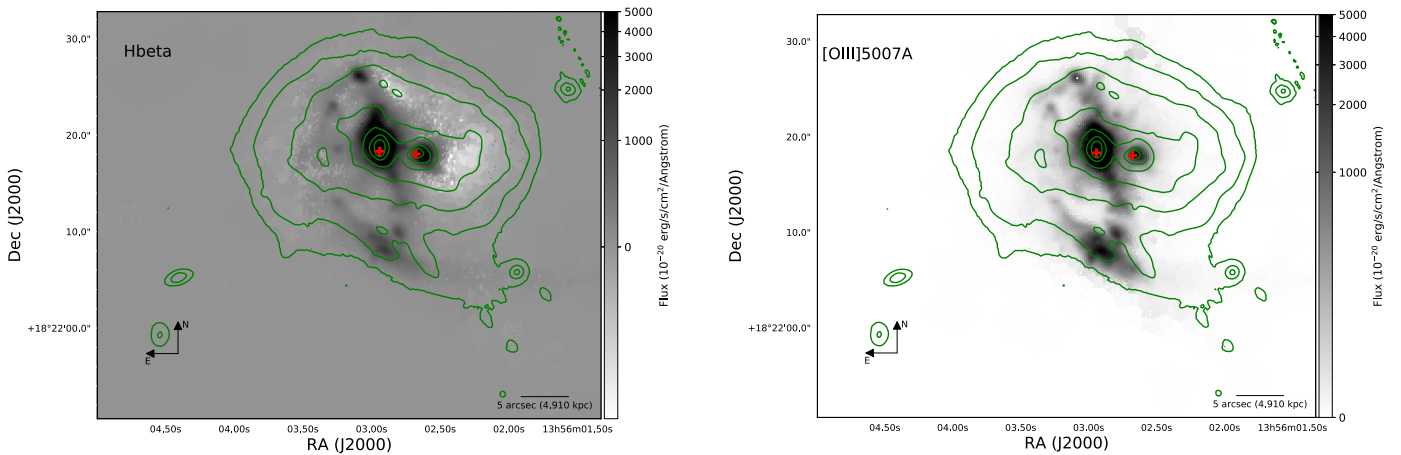


Figure 2. Flux distributions (grayscale) for the Mrk 463 system in the H β 4861 Å (left panel, ranging from -5×10^{-18} to 5×10^{-17} erg cm $^{-2}$ s $^{-1}$ to include the absorption features) and [O III] 5007 Å (right panel) atomic transitions. Fluxes, given in both cases in units of 10^{-20} erg cm $^{-2}$ s $^{-1}$, were measured in each pixel by summing the contribution from the Gaussian fit for each narrow component, with the profile given by the [O III] 5007 Å line, after subtracting the surrounding continuum. For reference, the red crosses show the location of the X-ray sources, while the green contours correspond to the optical continuum flux.

work. Further analysis, including emission line fitting, velocity maps, etc. of well-isolated narrow emission lines was carried out using IDL *Fluxer*²² tool version 2.7. More complex line fits, including several overlapping components were carried out using the Pyspeckit Python package (Ginsburg & Mirocha 2011), as Fluxer only allowed a maximum of two simultaneous Gaussian fits.

2.2. Sinfoni

We obtained near-IR IFU observations of Mrk 463 using the Spectrograph for Integral Field Observations in the Near Infrared (SINFONI; Eisenhauer et al. 2003) camera mounted at the VLT, as part of program 093.B-0513 (PI: S. Cales). This program aimed to observe four confirmed $z < 0.1$ dual AGN that are visible from the southern hemisphere, one of which was Mrk 463. SINFONI has a much smaller field of view, $8'' \times 8''$, and hence these observations only cover the central region around the dual nuclei.

The observations were carried out using the 125×250 mas spatial scale in seeing-limited mode (i.e., no adaptive optics), together with the *K*-band grating, which provides coverage from 1.95 to 2.45 μm and a spectral resolution of ~ 4000 . The observations were carried out in service mode and spread over four OBs: IDs 1053697 (2014 April 17), 1053700 (2014 May 17), 1053702 (2014 June 18), and 1053704 (2014 July 21). The requested weather conditions were: ambient seeing better than $0''.8$, clear skies and airmass < 1.5 . However, only OBs 1053697 and 1053700 met such conditions; the remaining ones were taken either in a worse seeing and/or in the presence of thin clouds. Therefore, for this analysis, we mostly focus on the first two OBs in order to achieve the highest possible image quality.

The reduction of the SINFONI data was carried out using the dedicated ESO pipeline version 2.9.0 (Modigliani et al. 2007) in *Reflex*. The following steps were performed: (i) creation of a map of non-linear pixels from flat-field frames obtained with increasing exposure times; (ii) creation of a combined dark frame and hot pixel map; (iii) creation of a master flat field from individual flat-field images; (iv) determination of the

optical distortion coefficients and computation of the slitlets' distance table; (v) creation of a wavelength map from a set of arc lamp observations in order to carry out the wavelength calibration; (vi) stacking of individual science and telluric star frames. The flux calibration of the science frames was performed using the Fitting Utility for SINFONI (*FUS*) package developed by Dr. Krispian Lowe as part of his PhD thesis,²³ based on observations of standard stars taken less than two hours away and with a difference in airmass < 0.2 from the science data. As in the case of the VLT/MUSE data, the final combined data cubes were analyzed using the QFitsview tool for a first-look visualization and Fluxer for the Gaussian fitting of each isolated emission lines.

2.3. ALMA

During ALMA Cycle 2, we were granted 5.1 hours of priority B time to observe a sample of four nearby dual AGN, including Mrk 463, in band 6 as part of program 2013.1.00525. S (PI: E. Treister). Four separate spectral windows were defined: one covering the $^{12}\text{CO}(2-1)$ molecular transition, providing a 10.7 km s^{-1} spectral resolution and a 2560 km s^{-1} bandwidth, and the remaining three covering the mm continuum at $\sim 220-235 \text{ GHz}$. The observations of Mrk 463 were taken on 2015 August 16 between 22:27 and 23:27 UT (uid://A002/Xa830fc/X4abc), and on 2015 September 16 between 21:01 and 22:01 UT (uid://A002/Xaa305c/X129). For the August 16th observations, 34 antennae were used, with baselines ranging from 43 m to 1.57 km, while on September 16th the same number of antennae were used, distributed between 41 m and 4.5 km baselines. The total on-target time in each observation was 25.7 minutes. Data reduction and analysis were carried out using the Common Astronomy Software Applications (CASA) version 4.5.0.

The requested 3σ sensitivity of the observations was $0.58 \text{ mJy beam}^{-1}$ per $\sim 10.7 \text{ km s}^{-1}$ channel. This requirement was not quite met, as the early processing carried out by the North America ALMA Science Center yielded a sensitivity of $0.78 \text{ mJy beam}^{-1}$ on the $^{12}\text{CO}(2-1)$ spectral window, 34% higher than the goal value. This value was obtained using a

²² <http://www.ciserlohe.de/fluxer/fluxer.html>

²³ Available at <http://uhra.herts.ac.uk/bitstream/handle/2299/2449/Krispian%20Lowe.pdf>.

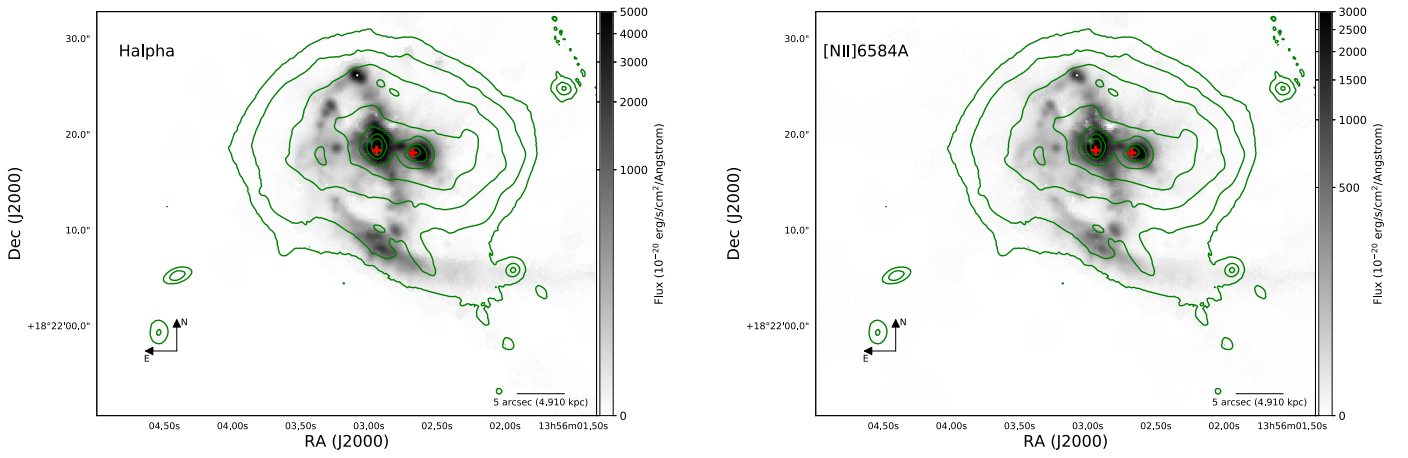


Figure 3. Emission maps (grayscale) for the $H\alpha$ 6563 Å (left panel) and the $[N II]$ 6583 Å (right panel) transitions obtained following the procedure described in the text. Contours, symbols, and units are the same as in Figure 2.

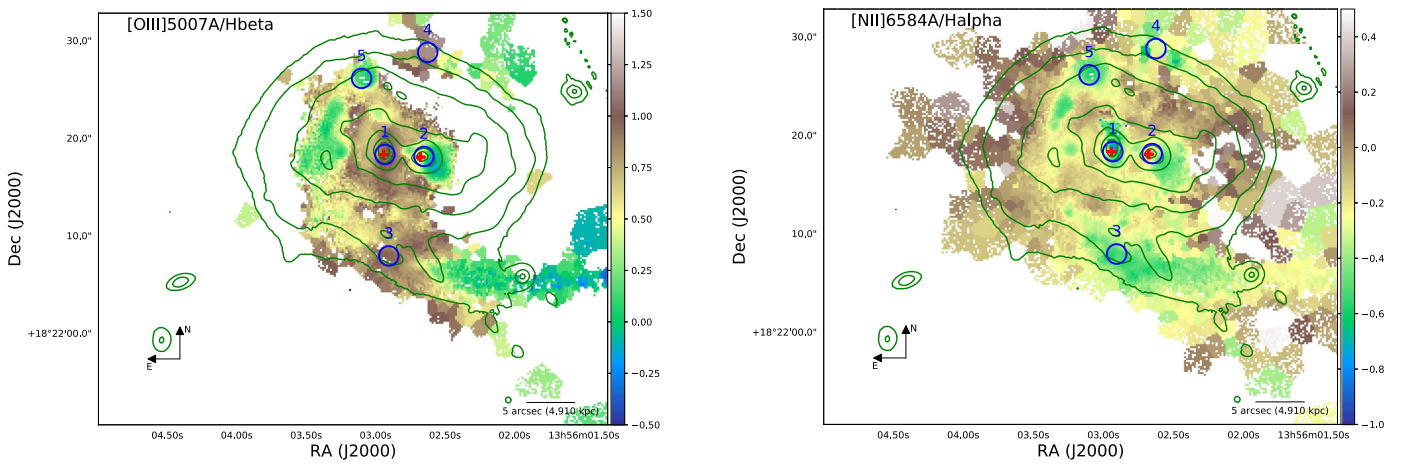


Figure 4. Map of the flux ratio between $[O III]$ 5007 Å and $H\beta$ 4861 Å (left panel) and $[N II]$ 6584 Å to $H\alpha$ 6563 Å (right panel) emission lines for the Mrk 463 system. Only pixels with a signal-to-noise ratio >3 in each respective line have been included. Green contours show the position of the integrated optical emission for reference, while the red crosses mark the hard X-ray emission. The five numbered blue circles show the regions in which the emission line ratios were measured and presented in Figure 6.

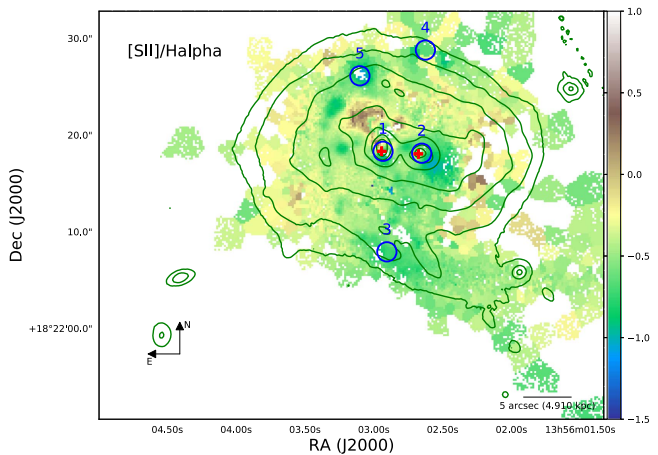


Figure 5. $[S II]$ to $H\alpha$ flux ratio for the Mrk 463 system. Contours and symbols are the same as in Figure 4.

Briggs Robust image weighting (Briggs 1995) with a robust parameter of 0.5, which provides a balance between a smaller beam and lower sensitivity. Instead, we decided to re-process

the ALMA data using a natural weighting scheme that delivers a higher sensitivity at the expense of a slightly worse spatial resolution. Using this method, we achieved a sensitivity of ~ 0.6 mJy beam $^{-1}$ at $3\text{-}\sigma$ in the $^{12}\text{CO}(2\text{-}1)$ line, thus coming much closer to our goal flux limit. The resulting beam size is $0''.3 \times 0''.17$.

2.4. Astrometric Calibration

In order to be able to compare emission at different wavelengths from the instruments described above, it is critical to ensure that all the data sets share the same astrometric reference point. This is potentially difficult, given the relatively small overlap in structures at different wavelengths. The ALMA absolute astrometric calibration is better than $\sim 0''.1$, as reported by González-López et al. (2017).

Using the *Chandra* X-ray data for this system, Bianchi et al. (2008) located the position of the two AGN to within $0''.5$. In particular, we derived the exact position using the hard X-ray band, 2–8 keV, because most of the emission can be attributed to the AGN in this case.

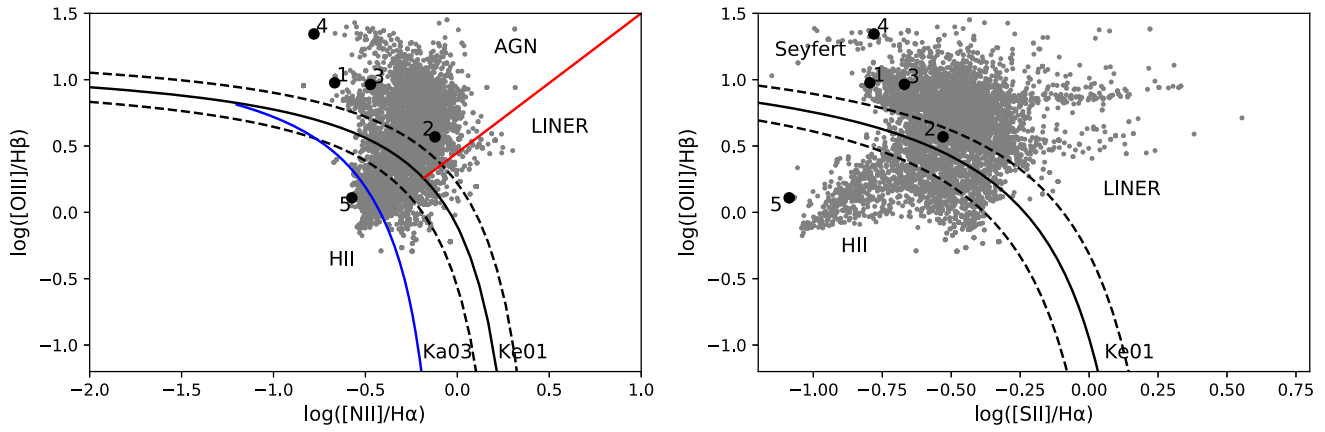


Figure 6. $[\text{N II}]/\text{H}\alpha$ vs. $[\text{O III}]/\text{H}\beta$ (left panel) and $[\text{S II}]/\text{H}\alpha$ vs. $[\text{O III}]/\text{H}\beta$ (right panel) diagrams for the five regions highlighted in Figure 4. The black solid curves show the separation between star-forming (H II) and active galaxies proposed by Kewley et al. (2001), while the adjacent dashed curves represent ± 0.1 dex of this relation, corresponding to the estimated error for this threshold. The red solid line on the left panel shows the separation between AGN and LINERs proposed by Schawinski et al. (2007), while the blue solid curve marks the classification threshold presented by Kauffmann et al. (2003). The background gray circles in both panels show the locations for all the Voronoi bins in Mrk463 with detected emission lines in this diagram. The black circles show the position of the highlighted regions in the system. As can be seen, regions 1–4 are clearly in the AGN zone, while position 5 can be classified as a star-forming region.

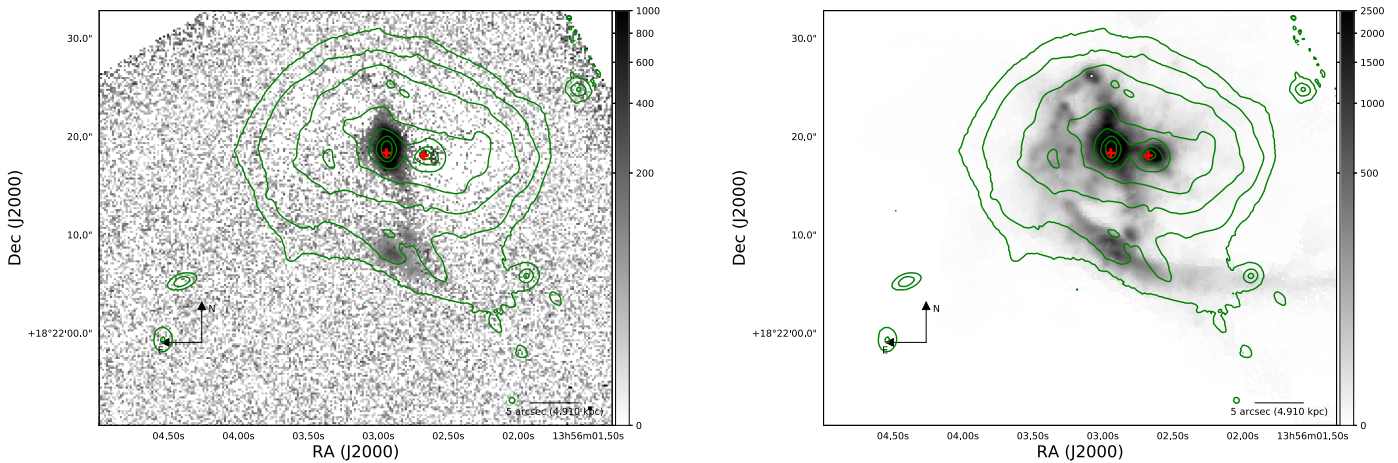


Figure 7. Flux maps for the He II 4685 Å (left panel) emission line and for the $[\text{S II}]$ 6717/31 Å doublet (right panel) obtained from the VLT/MUSE IFU data cubes. Contours, symbols, and units are the same as in Figure 2. Both maps were obtained by performing Gaussian fits to the emission lines.

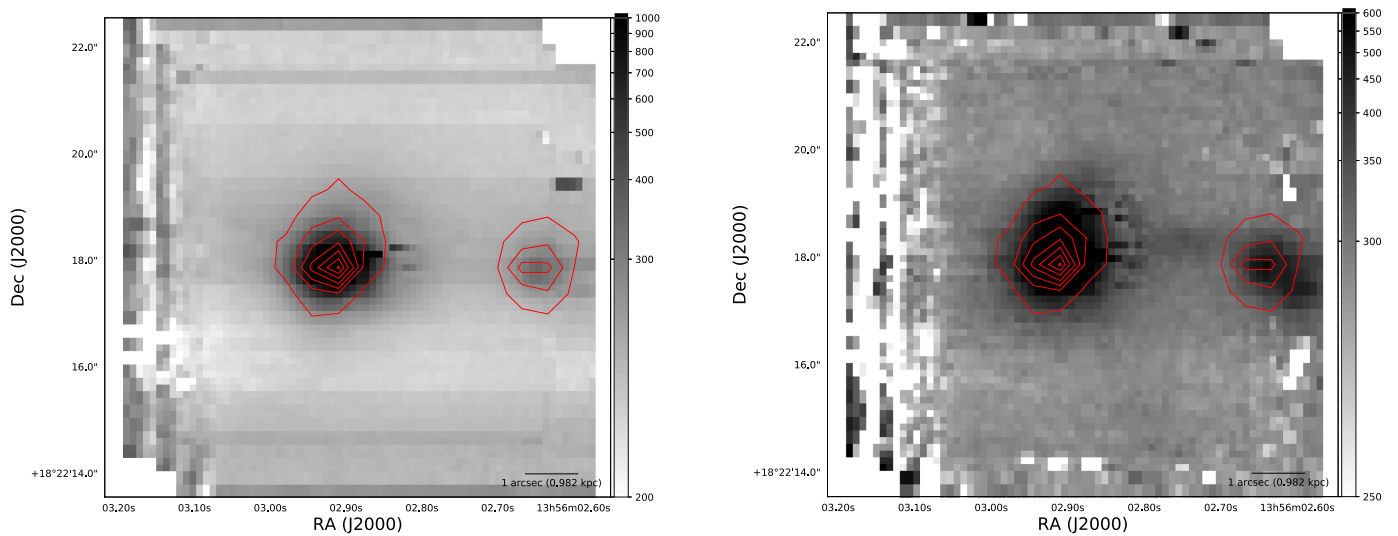


Figure 8. Left panel: Mrk 463 near-IR continuum at $\sim 2.2 \mu\text{m}$. Right panel: emission map for the Pa α hydrogen line at $1.8751 \mu\text{m}$. The VLT/SINFONI cubes were used to create these maps. The near-IR continuum was obtained by collapsing the data cube between 2.1 to $2.4 \mu\text{m}$ in the observed frame. The Pa α map was created by fitting a Gaussian function to the emission line after subtracting the surrounding continuum. Red contours in both cases show the hard X-ray emission detected by *Chandra*.

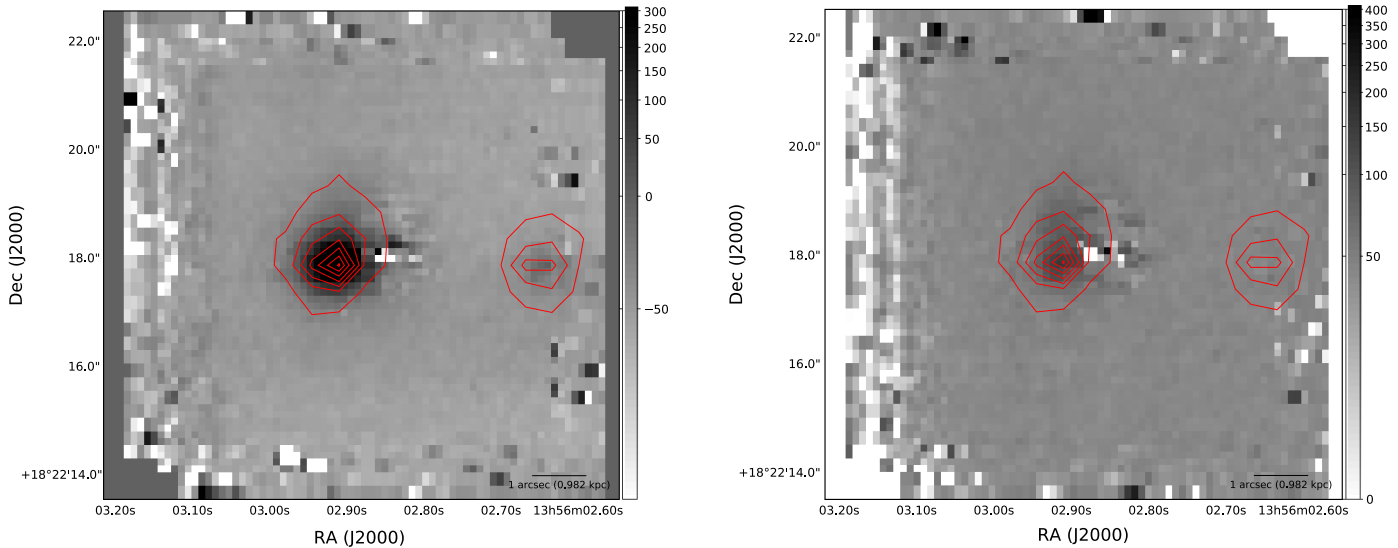


Figure 9. Left panel: emission map for the [Si VI] emission line at $1.962 \mu\text{m}$ in the rest frame. In this case, both nuclei are clearly detected. Right panel: image of the Hydrogen $\text{Br}\gamma$ emission at $2.1655 \mu\text{m}$ in the rest frame. The $\text{Br}\gamma$ appears to be significantly fainter, and hence only the Mrk 463E nucleus is detected—and at a much lower significance. Red contours in both cases show the hard X-ray emission detected by *Chandra*.

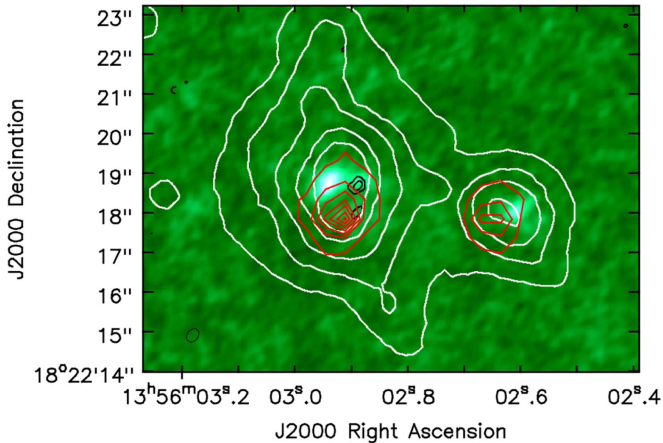


Figure 10. Mrk 463 ALMA $^{12}\text{CO}(2-1)$ emission integrated map. The black contours show the mm-continuum emission surrounding the $^{12}\text{CO}(2-1)$ line, while the red contours present the *Chandra* hard X-ray, 2–8 keV, emission and the white contours present the background-subtracted $\text{H}\alpha$ flux obtained from MUSE. The ellipse in the bottom left shows the beam size for the $^{12}\text{CO}(2-1)$ ALMA map.

3. Morphologies

Mrk 463 was morphologically classified as a peculiar/interacting galaxy based on early optical imaging (Adams 1977; Petrosian et al. 1978). Deeper CCD imaging by Hutchings & Neff (1989), which included a narrow-band filter covering the redshifted [O III] 5007 \AA emission lines, revealed extended emission in the Mrk 463E nucleus and a bright knot $\sim 10''$ south of the nucleus that are not visible in the optical continuum. Radio continuum observations at 6 and 20 cm performed by Mazzarella et al. (1991) show that the radio emission is aligned with the bipolar [O III] conical flows and the southern knot, strongly suggesting that they are connected to the Mrk 463E nuclear region.

In Figure 1, taking advantage of the MUSE IFU data, we present a reconstructed optical continuum image of the Mrk 463 system that ranges from ~ 4800 to $\sim 9300 \text{ \AA}$. This image covers the entire MUSE $\sim 1 \times 1 \text{ arcmin}^2$ field of view,

roughly an order of magnitude larger than previous IFU observations of this source (e.g., Chatzichristou & Vanderriest 1995). Both nuclei, Mrk 463E and Mrk 463W, are clearly visible on the image, together with the southern knot, which is almost exclusively seen in [O III] emission, as discussed in Section 3.1. Additionally, we can see relatively bright emission clumps, most prominently to the northeast of the Mrk 463E galaxy, which we will later, in the following subsection, associate with off-nuclear star-forming regions.

3.1. Optical Atomic Transitions

In order to obtain line flux maps from the MUSE data cubes, we perform Gaussian fits to the He II 4685 \AA , $\text{H}\beta$ 4861 \AA , [O III] 5007 \AA , $\text{H}\alpha$ 6563 \AA , [N II] $6548, 6583 \text{ \AA}$, and [S II] $6717, 6731 \text{ \AA}$ features. The line fitting procedure is as follows. First, the continuum emission in each pixel is subtracted by performing a fit using a second-order polynomial function between 5000 \AA and 8000 \AA . Using this broad wavelength range and a relatively small polynomial order allows to obtain a good fit for the spectral continuum in the region of interest while remaining unaffected by the presence of even prominent emission or absorption features. We then performed a Voronoi tessellation of the cube by demanding a minimal signal-to-noise ratio of 10 in the $\text{H}\alpha/[\text{N II}]$ complex in each bin. While this choice has no impact on the central regions of the system, where this condition is met basically on every pixel, it is important in the outskirts. We then assume Gaussian profiles for all emission lines. Given that it is a strong and well-isolated feature, we use the [O III] 5007 \AA line as a template in order to define the widths and relative wavelength offsets for all the subsequent narrow components. We further allow for a secondary line component at a different velocity, also using the [O III] 5007 \AA line as template and adding extra Gaussians with both the line centers and widths as free parameters to account for the possible presence of broad $\text{H}\alpha$ and $\text{H}\beta$ emission. In each case, a component is only considered if the peak is detected at a signal-to-noise greater than three.

The resulting images are presented in Figures 2 and 3. In all of these cases, the total flux for all the line components is

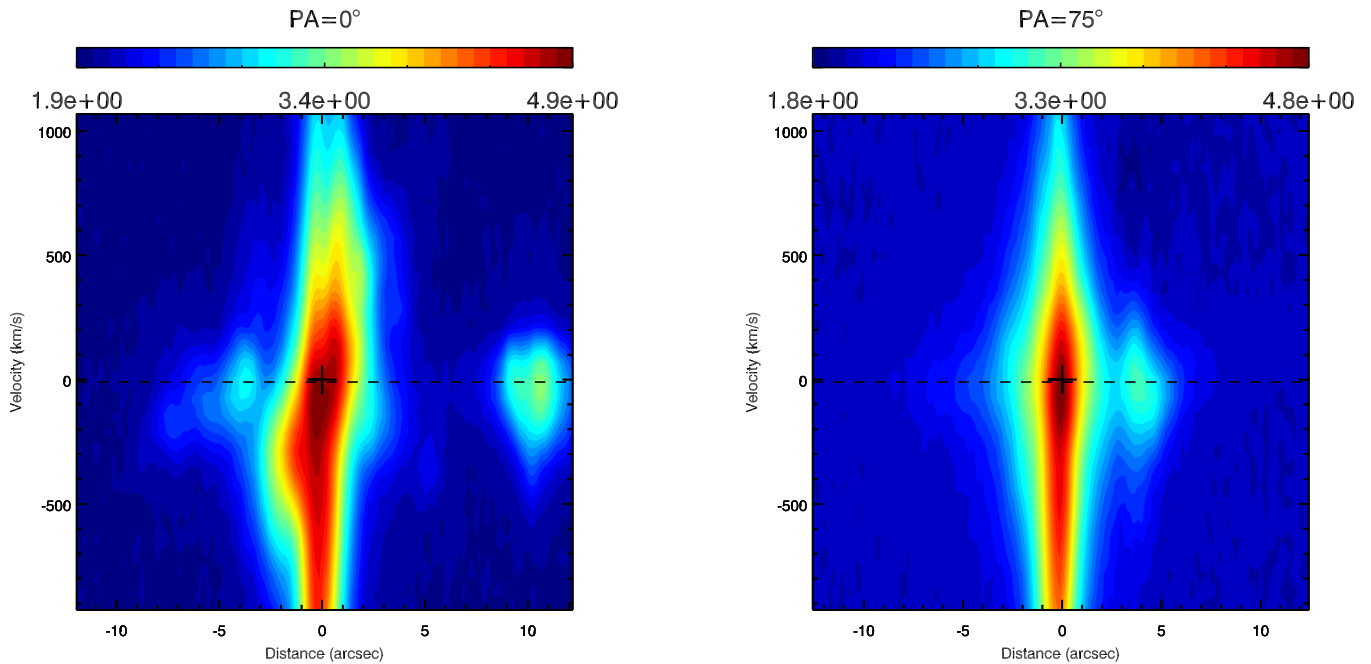


Figure 11. Position velocity ($p-v$) diagram for the [O III] 5007 Å emission line centered on the East nucleus. The left panel shows the emission along a north-south ($PA = 0^\circ$) slit, while the right panel uses a PA of 75° . The north-south slit falls directly on the position of the biconical outflow discussed below, which can be clearly visible, while no significant structures are visible on the 75° direction. About $10''$ away from the nucleus, on the $PA = 0^\circ$ diagram, we can see the southern emission region; on the $PA = 75^\circ$ slit, we can see part of the western nucleus at $\sim 4''$.

shown. Some of the same key features seen in Figure 1 and discussed in the previous section are clearly visible in these images as well. However, other remarkable components are now detected as well. Particularly important are the detections of extended $H\alpha$ gas to the northwest of the system and the “stream” of $H\alpha$ blobs to the southwest, seen in Figure 3. Additionally, we can identify an absorption region to the west of the Mrk 463W nucleus in the $H\beta$ 4861 Å map.

The flux ratios of these emission lines can be used in order to determine the nature of the ionization source (e.g., Baldwin et al. 1981; Veilleux & Osterbrock 1987; Kewley et al. 2006). Figures 4 and 5 show the maps for the [O III]/ $H\beta$, [S II]/ $H\alpha$, and [N II]/ $H\alpha$ ratios, computed using the sum of the flux in the narrow components for each emission line. According to Kewley et al. (2006), any source/region with [O III]/ $H\beta$ > 10 is nearly guaranteed to be dominated by AGN ionization, independent of the value of [N II]/ $H\alpha$ or [S II]/ $H\alpha$. While shocks appear to be widespread in major galaxy mergers, they typically have lower [O III]/ $H\beta$ ratios, $\sim 1-5$, compared to active nuclei (Rich et al. 2011, 2015). Hence, just from examination of Figure 4, we can see several potential AGN-dominated regions. In order to investigate the nature of the ionization energy source(s), we selected five outstanding zones in the system, highlighted in Figures 4 and 5: the two nuclear regions, the southern emission line region, the northern clump, and a representative $H\alpha$ emitting region in the northwest. The locations of these five regions on the [O III]/ $H\beta$ versus [N II]/ $H\alpha$ and [S II]/ $H\alpha$ diagnostic diagrams are shown in Figure 6. As can be clearly seen, both nuclei, the southern emission line region, and the northern clump are consistent with being dominated by the AGN energy output. In contrast, region #5 appears to fall on the star-forming locus. These diagrams indicate that the influence of the AGN on the surrounding material is widespread and can be detected at large distances, even ~ 10 kpc away from the nuclei.

Further hints about the nature of the ionization sources in this system can be obtained by exploring emission lines with higher ionization energies. To this end, Figure 7 shows the emission maps for the He II 4685 Å and [S II] 6717/31 Å lines, which have ionization energies of 54.4 eV and 23.3 eV, respectively. As can be seen in the figure, highly ionized lines, particularly He II, are much more concentrated, mostly on the Mrk 463E nucleus and the emission line regions, while Mrk 463W is barely detected. As presented by Shirazi & Brinchmann (2012) and later by Bär et al. (2017), the He II 4685 Å emission and He II/ $H\beta$ ratio can be used to identify AGN even in sources missed by classification methods based on emission lines at lower ionization energies (Sartori et al. 2015). According to Shirazi & Brinchmann (2012), sources or regions with $\log(\text{He II}/H\beta) > -1$ can be classified as AGN dominated. This is the case for the Mrk 463E nucleus and its surrounding ionization cone, for the southwest emission line region but not for the Mrk 463W nucleus. This suggests that the AGN in Mrk 463E is energetically more important for the system than the one in Mrk 463W.

3.2. Near-IR Maps

Although the VLT/SINFONI near-IR IFU data only cover a smaller $\sim 8'' \times 8''$ region at the center of the Mrk 463 system, as shown in Figure 1, they are an important complement to the MUSE optical maps. Figure 8 shows the near-IR continuum between 2.1 and 2.4 μm and the continuum-subtracted integrated Pa α hydrogen emission line at 1.8751 μm in the rest frame. For this and all other near-IR emission lines, the continuum subtraction was carried out by performing a simple first-order polynomial fit to the adjacent spectral regions on each side of the line. The line fitting was carried out assuming a single Gaussian functional form, which was visually deemed appropriate and reasonable, considering that the SINFONI data

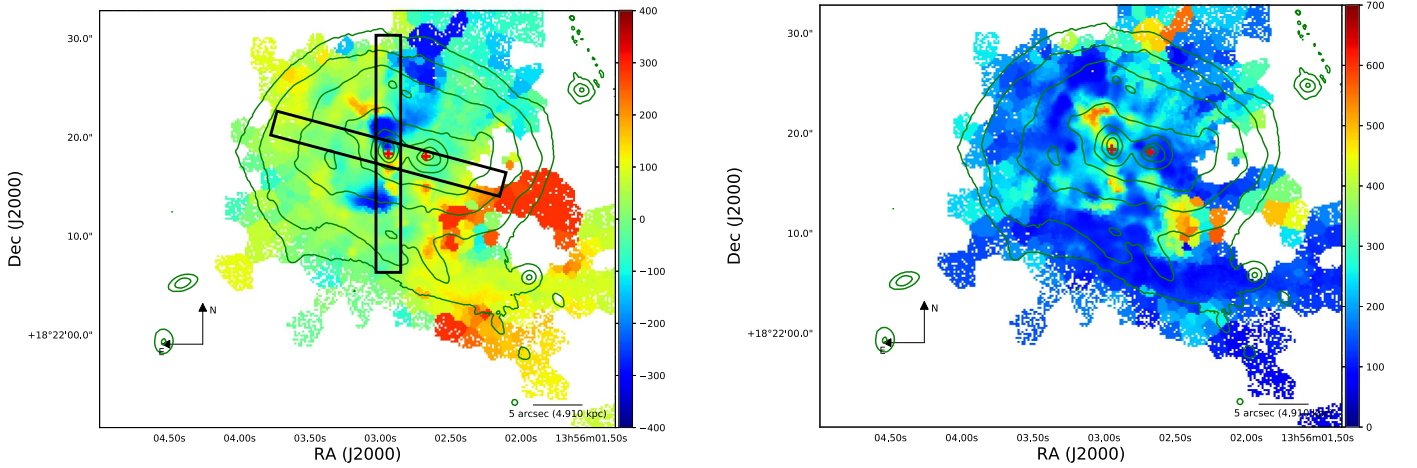


Figure 12. Left panel: velocity map for the [O III] 5007 Å line, measured in km s^{-1} relative to the systemic velocity at the redshift of the system ($z = 0.050355$). Contours and symbols are the same as in Figure 2. Black rectangles show the location of the slits used for the p - v diagrams presented in Figure 11. Right panel: velocity dispersion map for the [O III] 5007 Å line. Contours are the same as in the left panel.

only cover the central region of the system. No cut in signal to noise ratio of the resulting line was used in constructing the map. Both nuclei are clearly detected on the continuum map, showing a very similar morphology to the optical continuum image presented in Figure 1. The $\text{Pa}\alpha$ map, in contrast, reveals new components. In particular, we can marginally detect an emission blob between the two nuclei and another emitting region to the west of the Mrk 463W nucleus. While both of these regions are also visible in the $\text{H}\alpha$ map, they are not detected in [O III], suggesting that they are star-forming regions. However, as will be later shown in Section 5.1, the region between the nuclei is subject to moderate extinction, $A_{\text{H}\alpha} \sim 2$, and therefore it is possible that the lack of detection of [O III] in this area is due to obscuration.

The $\text{Pa}\alpha$ emission line provides a measurement of the star formation rate. Using the SINFONI cube, together with the conversion from $\text{Pa}\alpha$ luminosity to star formation rate provided by Rieke et al. (2008), we derive values of $26.5 M_{\odot} \text{ yr}^{-1}$ for the East nucleus and $0.75 M_{\odot} \text{ yr}^{-1}$ for the West one. These star formation rates derived from the $\text{Pa}\alpha$ line are fully consistent with those of $30 M_{\odot} \text{ yr}^{-1}$ for Mrk 463E and $<10 M_{\odot} \text{ yr}^{-1}$ for Mrk 463W reported by Evans et al. (2002). However, it is important to point out that, as shown in Figure 6, both nuclei appear to be dominated by the AGN emission, at least for the optical lines, and thus these SFR estimates can be considered as upper limits.

The near-IR data also map other emission lines such as [Si VI] and Hydrogen $\text{Br}\gamma$ at rest-frame wavelengths of 1.962 and $2.1655 \mu\text{m}$, respectively; these are both presented in Figure 9. Emission from [Si VI] is detected at high significance from Mrk 463E and weakly from Mrk 463W, thus further confirming the AGN nature of both nuclei. However, in contrast, $\text{Br}\gamma$ is only weakly detected from Mrk 463E.

3.3. CO and Dust Continuum

With our ALMA Cycle 2 data, we detect both $^{12}\text{CO}(2-1)$ and the mm continuum in the central region of the Mrk 463 system. Figure 10 shows the velocity-integrated continuum-subtracted $^{12}\text{CO}(2-1)$ emission map, together with contours for the rest-frame 232 GHz continuum. As can be seen, the strongest $\text{CO}(2-1)$ emission is found in a region to the northeast of the Mrk 463E nucleus, although significant

emission is also located around each nucleus, as well as between them. Interestingly, only a small fraction of the $\text{CO}(2-1)$ emission overlaps with the AGN location.

Defining a $\sim 4'' \times 3''$ region centered on the Mrk 463E nucleus that encloses the majority of the flux, we obtain a total flux density of $11.4 \pm 0.12 \text{ Jy km s}^{-1}$. In this case, the error bars were estimated by measuring the rms in nearby source-free regions of the same area. Previous observations of this source at lower resolution, $\sim 2''$, yielded total unresolved fluxes of $7.2 \pm 0.8 \text{ Jy km s}^{-1}$ (Alloin et al. 1992) and $6.8 \pm 0.9 \text{ Jy km s}^{-1}$ (Evans et al. 2002) for the $^{12}\text{CO}(1-0)$ transition. Following Solomon & Vanden Bout (2005), we assume that the CO emission is thermalized and optically thick, such that the intrinsic line luminosity is independent of J , and hence we expect the $^{12}\text{CO}(2-1)$ flux density to be four times higher than $^{12}\text{CO}(1-0)$. Therefore, our high-resolution ALMA observations resolve $\sim 50\%$ of the CO emission for the Mrk 463E nucleus extended over scales of $\sim 4''$. Using a region of the same area centered on the Mrk 463W nucleus, we derive a line flux density of $4.5 \pm 0.12 \text{ Jy km s}^{-1}$. This is consistent with the estimates of Evans et al. (2002), who also found a flux ratio of $\sim 3:1$ between the Mrk 463E and Mrk 463W nuclei, thus suggesting that the extended component encompasses both nuclei—as expected, given the observed nuclear separation.

Following the prescription described in Sections 2.1 and 2.2 of Solomon & Vanden Bout (2005), particularly their Equation (3):

$$L'_{\text{CO}} = 3.25 \times 10^7 S_{\text{CO}} \Delta v \nu_{\text{obs}}^{-2} D_L^2 (1+z)^3,$$

we calculate a $\text{CO}(2-1)$ luminosity for the emission surrounding the Mrk 463E nucleus of $L'_{\text{CO}(2-1)} = 3.173 \times 10^8 \text{ K km s}^{-1} \text{ pc}^2$. Next, using the relation $M_{\text{gas}} = M(\text{H}_2) = \alpha L'_{\text{CO}}$, and $\alpha = 4.3 M_{\odot} (\text{K km s}^{-1} \text{ pc}^2)^{-1}$ (Bolatto et al. 2013), we obtain a total gas mass in this region of $1.36 \times 10^9 M_{\odot}$. Similarly, for the material surrounding the Mrk 463W nucleus, we obtain $L'_{\text{CO}(2-1)} = 1.253 \times 10^8 \text{ K km s}^{-1} \text{ pc}^2$ and $M_{\text{gas}} = 5.39 \times 10^8 M_{\odot}$. These differ from the gas masses derived by Evans et al. (2002), primarily due to the different values of α assumed. Indeed, Evans et al. (2002) used a value of $\alpha = 1.5 M_{\odot} (\text{K km s}^{-1} \text{ pc}^2)^{-1}$ for this source and reported a total molecular gas mass of $10^9 M_{\odot}$, whereas we obtain $\sim 7 \times 10^8 M_{\odot}$ while assuming their α value.

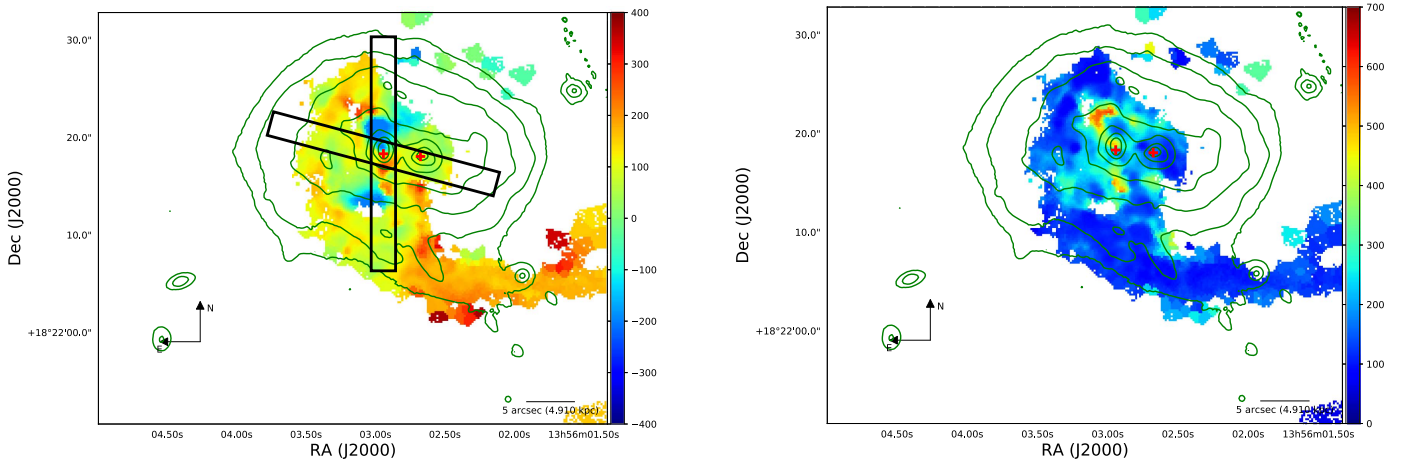


Figure 13. Left panel: $H\beta$ 4861 Å velocity map in km s^{-1} relative to the systemic velocity. Contours show the $H\beta$ 4861 Å flux, as measured from our Gaussian fitting of the line, presented in Figure 2. Black rectangles show the location of the slits used for the p - v diagrams presented in Figure 11 Right panel: $H\beta$ 4861 Å velocity dispersion map in km s^{-1} . Contours are the same as in the left panel.

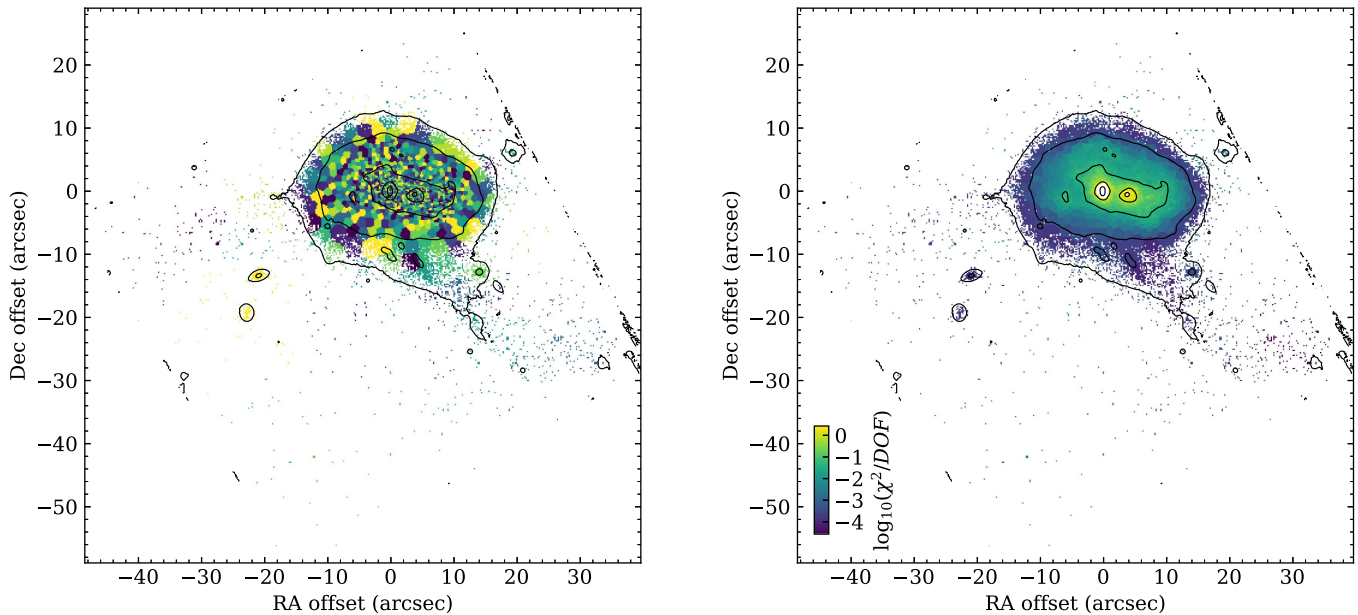


Figure 14. Left panel: Voronoi tessellation binning of the Mrk 463 VLT/MUSE data, requiring a minimum SNR of 30. The black contours were obtained from the white light (integrated) VLT/MUSE image, presented in Figure 1. The lowest contour is at $2 \times 10^{-20} \text{ erg s}^{-1} \text{ cm}^{-2} \text{ Å}^{-1}$, while the contours increase as $2''$. The coordinates are given relative to the position of the Mrk 463E nucleus at 13:56:02.92, 18:22:18.1. Right panel: reduced χ^2 map for the stellar population fits. Contours and coordinates are the same as in the left panel. Fits were not performed in the nuclear regions, as the emission is strongly dominated by the AGN in these areas.

4. Kinematics

The multi-wavelength IFU data for Mrk 463 can be used to trace both absorption and emission lines, as well as to measure the kinematics of the system.

4.1. Optical Emission Lines

Using the VLT/MUSE data, we analyze the kinematics from two strong and well-isolated emission lines: $H\beta$ 4861 Å and $[O III]$ 5007 Å. Figure 11 shows the position-velocity (p - v) diagram centered on the Mrk463-E nucleus with position angles (PAs) of 0° (i.e., north-south) and 75° using the $[O III]$ 5007 Å line. In this case, we assume a reference velocity of 15226 km s^{-1} , which is 130 km s^{-1} higher than the systemic heliocentric velocity of 15096 km s^{-1} that corresponds to the redshift of 0.050355 reported by Falco et al. (1999), which we

used for the rest of the analysis. This was done to match the center of the potential additional stellar disk to the west of Mrk 463W discussed in Section 4.2. A clear velocity gradient can be seen on the north-south slit, as discussed below. This structure is very spatially localized, as it is not present on the $PA = 75^\circ$ diagram. The southern emission line is visible on the $PA = 0^\circ$ slit region at $\sim 10''$. As can be seen, this region is roughly at the systemic velocity. Similarly, part of the emission associated with the Mrk463W nucleus can be seen on the $PA = 75^\circ$ diagram, at $\sim 4''$ away from the eastern one.

Figure 12 shows the velocity and velocity dispersion maps for the $[O III]$ 5007 Å emission line. The velocity gradient associated with the eastern nucleus that was visible on the p - v diagram shown in Figure 11 is present here as well. As first suggested by Hutchings & Neff (1989) and later discussed by Chatzichristou & Vanderriest (1995), this structure is consistent

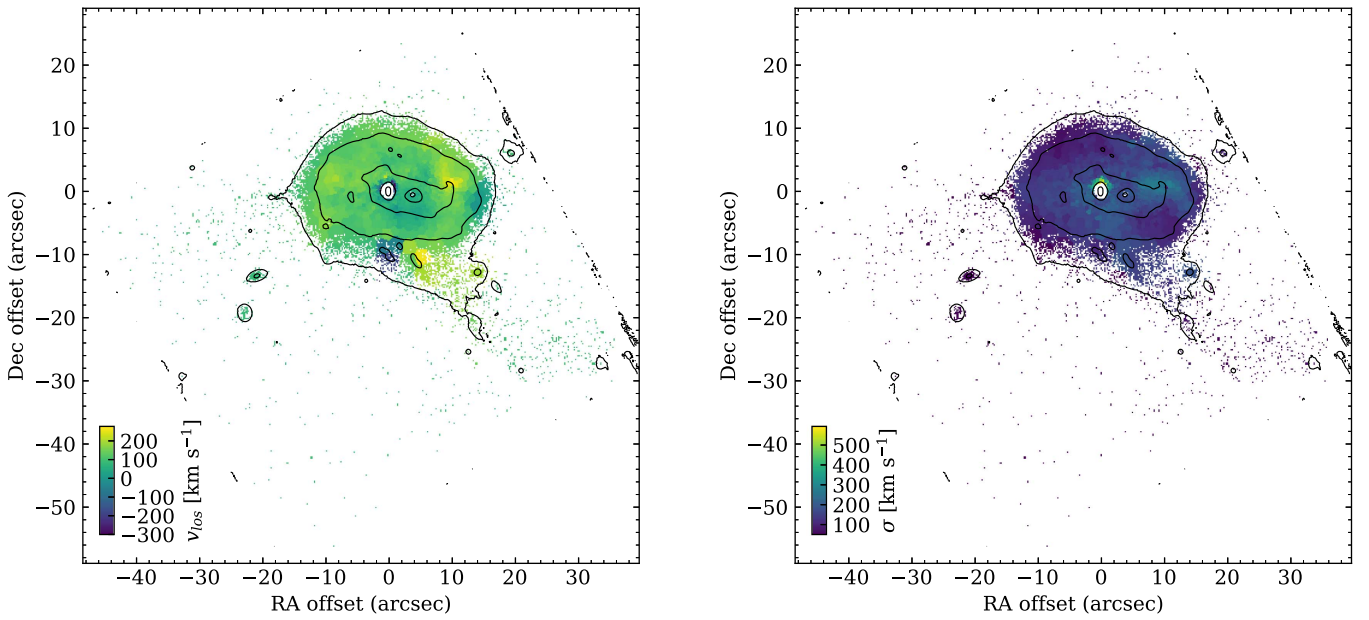


Figure 15. Stellar velocity (left panel) and velocity dispersion (right) maps for the Mrk 463 system, in km s^{-1} . Contours and coordinates are the same as in Figure 14.

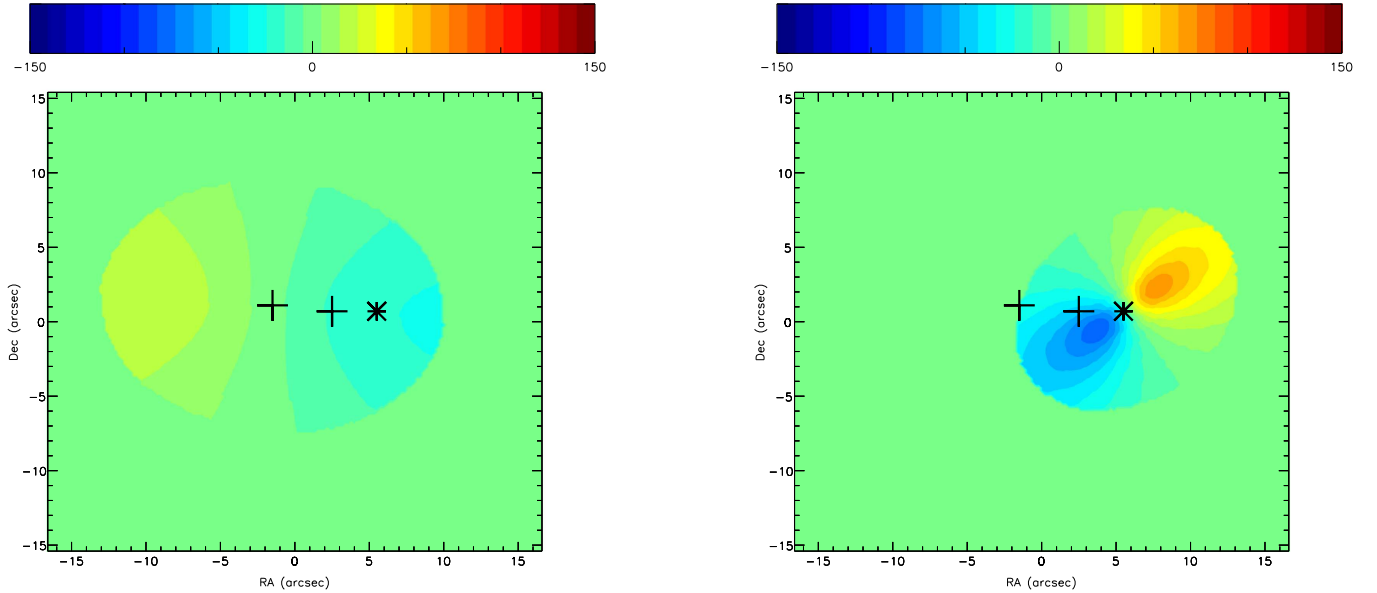


Figure 16. Keplerian disk models used to fit the stellar kinematic maps shown in Figure 15. Crosses show the positions of the two nuclei. Two disks were fitted, one centered on the Mrk 463E nucleus and a PA of 75° (left panel) and a second one centered in the position marked by the asterisk and a PA of 125° (right panel).

with the presence of a two-sided ionization cone, which also aligns with the extended radio emission detected from this nucleus. While a detailed modeling of this biconical outflow is beyond the scope of this paper, we can use the observed emission line features in this region to derive physical properties of the ionized gas outflow. As presented by Müller-Sánchez et al. (2011), the mass outflow rate is given by

$$\dot{M}_{\text{out}} = 2m_p n_e v_{\text{max}} A f,$$

where m_p is the proton mass, n_e is the density of the ionized gas, A is the lateral surface area of one cone of the outflowing region, and f is the filling factor of the ionized gas. The factor of two accounts for the two sides of the ionized cone. The value of n_e can be estimated from the observed ratio of the [S II]

6716/6731 Å emission lines, as described by Osterbrock & Ferland (2006). We find that, on average, the [S II] ratio in the region of the biconical outflow has a value ~ 0.7 . According to the prescription of Osterbrock & Ferland (2006) and assuming a temperature of $\sim 10,000$ K, we estimate that n_e should be in the range from 1000 to 5000 cm^{-3} and adopt a value of 3000 cm^{-3} . For the filling factor, f , which cannot be derived directly from observations, a range of $0.01 < f < 0.1$ is commonly assumed (e.g., Storchi-Bergmann et al. 2010). However, our assumed n_e value is much higher than in those cases, and considering the $n_e \propto f^{-0.5}$ relation proposed by Oliva (1997), we assume a value of $f = 0.001$, which is 10 times larger than the value used by Nevin et al. (2018). We consider a maximal velocity of $v_{\text{max}} = 350 \text{ km s}^{-1}$, as

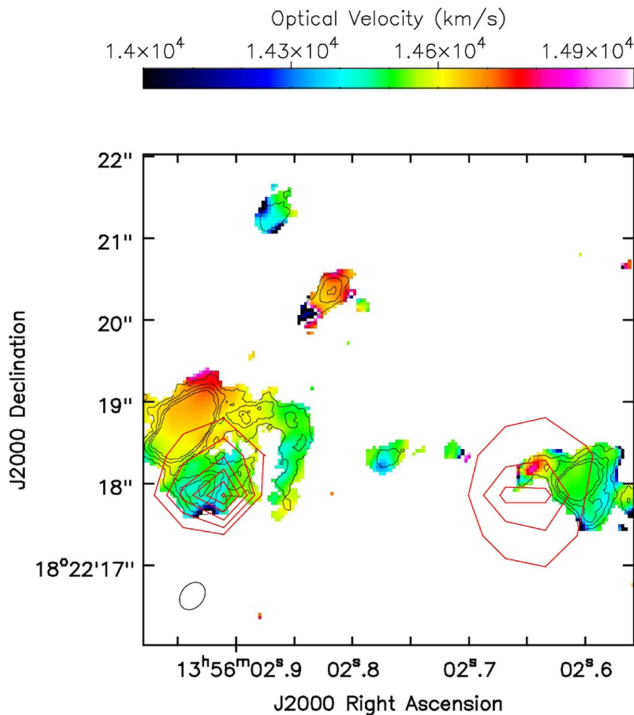


Figure 17. $^{12}\text{CO}(2-1)$ velocity map. Only regions with emission at >0.07 mJy beam $^{-1}$ km s $^{-1}$ are included in the map. Red contours correspond to the *Chandra* hard X-ray, 2–8 keV, emission.

measured on the [O III] velocity map. The value of A is obtained considering that the physical distance from the nucleus to the location of the maximal velocity is $\simeq 3.3$ kpc and that the cone radius at that position is $\simeq 0.9$ kpc, thus yielding $A = 9.62 \times 10^6$ pc 2 . Next, using the expression described above, we obtain that $\dot{M}_{\text{out}} = 512(f/0.001) M_{\odot} \text{ yr}^{-1}$. This value is on the high side of the range of mass outflow rates found previously in systems hosting biconical outflows (Müller-Sánchez et al. 2011, 2016; Nevin et al. 2018) in moderate-luminosity AGN and similar to those found in high redshift quasars (Brusa et al. 2015) and ULIRGs (e.g., Veilleux et al. 2005).

In addition, we also detect a rapidly outflowing region to the northwest of the Mrk 463E nucleus, reaching speeds of up to ~ -600 km s $^{-1}$. This region was already identified as #4 in Figure 4. As shown in Figure 6, this region has the highest value of the [O III]/H β ratio and is clearly located in the AGN region, which confirms that this outflowing material is being ionized by the AGN, most likely in Mrk 463E, given its spatial location and the luminosity of its nucleus. Furthermore, this outflowing region appears to be spatially connected to the biconical outflow. The velocity dispersion map for the [O III] 5007 Å line shows a broad emission line component in the central region of Mrk 463E. Both the north and south edges of the biconical outflows also show relatively high-velocity dispersions, reaching up to ~ 600 km s $^{-1}$, suggesting the presence of shocks in the boundary of the outflowing regions. The remaining regions are characterized by relatively low-velocity dispersions, up to ~ 200 km s $^{-1}$, close to the spectral resolution of VLT/MUSE.

The velocity and velocity dispersion maps, as measured from the H β 4861 Å emission line, are shown in Figure 13. As for the [O III] 5007 Å line, a very clear gradient, ranging from

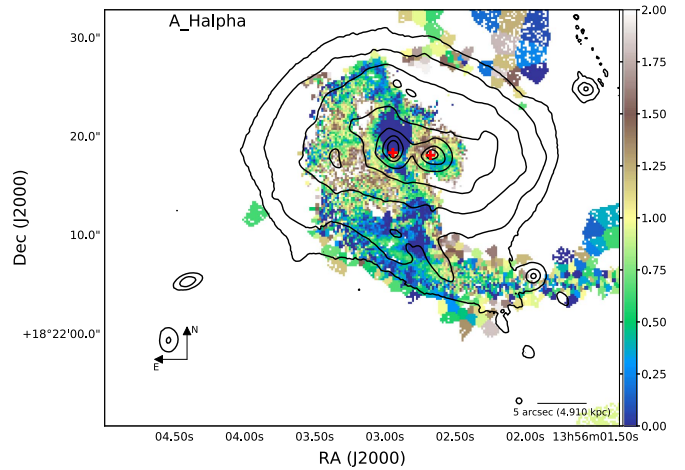


Figure 18. Optical extinction map for the Mrk 463 system derived from the H α /H β flux ratio, as described in the text. Black contours show the optical continuum flux, while the red crosses mark the location of the hard X-ray sources detected by *Chandra*. The map shows that, while most of the system is characterized by relatively low extinction levels, $A_{\text{H}\alpha} < 1$, some specific regions, most notably in between the two nuclei, can reach moderate absorption levels up to $A_{\text{H}\alpha} \sim 2$.

-350 km s $^{-1}$ in the north to ~ 150 km s $^{-1}$ in the south, centered on the Mrk 463E nucleus, is clearly visible. This gradient is also associated with the biconical outflow presented above. This map does not include the absorption line region located to the west of the Mrk 463W nucleus, which will be studied in detail in the following subsection. Both nuclei appear to be consistent with the systemic velocity, or with very small offsets. Similarly, the southern emission line region is at the systemic velocity and has no discernible structure. However, there is a clear tail of atomic gas emission traced by the H β 4861 Å transition, which includes the southern emission line region visible in the [O III] map, presenting a velocity gradient ranging from ~ 100 km s $^{-1}$ to >200 km s $^{-1}$. This appears to reflect the velocity gradient along a tidal tail from the ongoing dynamical interaction and is consistent with the velocity gradient seen in HI observations of other systems (e.g., Hibbard & van Gorkom 1996).

The velocity dispersion profile for the H β 4861 Å line reveals the presence of a relatively broad component with an FWHM of up to ~ 700 km s $^{-1}$ in the nuclear region Mrk 463E, consistent with the location of the hard X-ray emission reported by Bianchi et al. (2008). The arc-like structure to the northeast of the Mrk 463E, which also shows high-velocity dispersion values, is explained by the presence of two superimposing velocity components, one associated with the edge of the biconical outflow reaching velocities of ~ 400 km s $^{-1}$ and the underlying galaxy at the systemic velocity. The rest of the system presents only narrow components with a width of ~ 200 km s $^{-1}$ or less, consistent with being unresolved at the MUSE spectral resolution.

4.2. Stellar Kinematics

We can further use the VLT/MUSE data cube to measure the kinematic properties of the stars in the Mrk 463 system. In order to achieve this, we performed a new Voronoi tessellation (Cappellari & Copin 2003), this time aimed to reach a minimum signal-to-noise ratio of 30 per bin in the optical continuum near the Mg b feature at ~ 5200 Å in the rest frame. The resulting bin map is shown in Figure 14. Next, for each

bin, we simultaneously masked the most prominent emission lines and fitted the optical continuum and absorption lines using the Penalized Pixel-Fitting (pPXF) method presented by Cappellari & Emsellem (2004). The optical spectrum at each Voronoi bin was fitted using stellar templates from the MILES library (Falcón-Barroso et al. 2011), which were then used to derive properties such as the stellar velocity and velocity dispersion, h_3 and h_4 Hermite polynomial coefficients, etc. A more detailed description of this procedure is given by Cappellari (2017). In Figure 14, we show the reduced χ^2 for each Voronoi bin. Fits were not obtained for the central regions of each galaxy, as the optical spectra in these are dominated by AGN light.

In Figure 15, we present the stellar velocity and velocity dispersion maps created by performing this spectral fitting. While the stellar velocity map appears rather flat, some structures are visible. In particular, there is a clear region to the northwest of the Mrk 463W nucleus, presenting a relative line-of-sight velocity of $\sim 200 \text{ km s}^{-1}$. In addition, a negative velocity region can be observed to the south of the Mrk 463W nucleus. These features could potentially be related to the ongoing major merger, such as tidal plumes from a second (or later) close pass of the nuclei. Interestingly, this structure overlaps spatially with a region dominated by $H\beta$ in absorption, as can be seen in Figure 2. This, together with the fact that this region does not have a counterpart on the emission line velocity maps presented in Figures 13 and 12, strongly suggests that this region is mostly devoid of ionized gas. While very faint, this structure can be seen as an extra component in the optical continuum, as shown in Figure 1.

The stellar population fit simultaneously constrains the line-of-sight stellar velocity dispersion, which is presented on the right panel of Figure 15. As for the velocity map, the velocity dispersion in the Mrk 463 system appears to be rather flat and featureless. Again, the region to the northwest of the Mrk 463W nucleus presents an elevated value for the stellar velocity dispersion of $\sim 400 \text{ km s}^{-1}$, while the average for the system is $\sim 100 \text{ km s}^{-1}$. This broadening in the line-of-sight velocity dispersion may be evidence of multiple velocity components at this location, perhaps due to the superposition of a secondary tidal tail against a potential stellar disk.

In order to explore the existence of potential disk(s) revealed by kinematical structures, we attempt to fit the stellar kinematics with disk models. Specifically, we use the Keplerian disk models presented by Bertola et al. (1998). We use two disks, one centered on the Mrk 463E nucleus and the other at the center of the velocity gradient found to the west of Mrk 463W. Spatial profiles of the two models are presented in Figure 16. The models fit the data reasonably well, leaving only small velocity residuals. Hence, it is possible to explain the Mrk 463 system as a combination of a bulge and a faint extended disk associated with Mrk 463E, together with a bulge centered on Mrk 463W and a gas-stripped stellar disk to the west of Mrk 463W. There does not seem to be any connection between the ionized gas outflows discussed in Section 4.1 and the potential stellar disks presented here. As discussed in Section 4.1, the outflows in this system appear to be mostly located in the north–south direction and originate from the Mrk 463E nucleus. In contrast, the Mrk 463E stellar disk is oriented with a PA of 75° , i.e., mostly east–west. Similarly, the presumed stellar disk to the west of Mrk 463W does not appear to be connected in any obvious way to any ionized gas outflow.

As described above, we would like to further emphasize that it is also possible to understand the observed structures in the stellar kinematics maps via the dynamical effects of the ongoing major galaxy mergers, which is also more natural because it does not require us to assume an ad hoc stellar disk offset by $\sim 3 \text{ kpc}$ from the nucleus of the galaxy. Unfortunately, separating these two scenarios requires observations at higher spectral resolutions than those that can be provided by VLT/MUSE over relatively large angular scales necessary to cover the whole system.

4.3. CO and Dust Continuum

Thanks to the ALMA data, we can analyze the molecular gas kinematics in the nuclear regions of the Mrk 463 system. Figure 17 shows the $^{12}\text{CO}(2-1)$ velocity map. Interestingly, the molecular gas regions around each nucleus show very clear velocity gradients, with a range of $\sim 800 \text{ km s}^{-1}$ in the case of the east region and $\sim 400 \text{ km s}^{-1}$ next to the west region. Smaller gradients can be seen in a few other locations, including the one between the two nuclei.

The eastern emission region presents an incomplete ring-like or infalling spiral structure, possibly centered on the AGN, based on the X-ray position. While there is relatively little $\text{CO}(2-1)$ emission detected directly on top of the nucleus, we can use the gas mass and velocity in the immediate vicinity of Mrk 463E to obtain an estimate of the gas infall rate on scales of $\sim 300 \text{ pc}$ around the SMBH. Considering only the material in the central ALMA beam, corresponding to ~ 0.3 or 300 pc or a 150 pc radius, we obtain a total CO mass of $\sim 3.8 \times 10^7 M_\odot$. Now, assuming that this gas is falling at $\sim 200 \text{ km s}^{-1}$ (based on the $\text{CO}(2-1)$ velocity measured on the nuclear ALMA beam) and that it is at an average distance of 75 pc , this yields an influx rate of $\sim 104 M_\odot \text{ yr}^{-1}$. While merely an approximation, this value is over three orders of magnitude larger than the accretion rate of $\sim 0.017 M_\odot \text{ yr}^{-1}$ inferred from the X-ray luminosity of the Mrk 463E nucleus reported by Bianchi et al. (2008). This situation is very similar to what was found in the local AGN NGC1068 by Müller Sánchez et al. (2009) and later confirmed by García-Burillo et al. (2014) using high-resolution ALMA data, thus strongly suggesting that SMBH accretion is a highly inefficient process that requires the infalling material to lose most of its angular momentum.

5. Discussion

5.1. Optical Extinction

Major galaxy mergers are known for potentially being subject to significant extinction, particularly at optical and UV wavelengths (e.g., Trentham et al. 1999; Bekki & Shioya 2000). Spectroscopically, the traditional way to estimate the amount of optical extinction is based on the observed ratio between the $H\alpha$ and $H\beta$ lines (e.g., Caplan & Deharveng 1986; Maíz-Apellániz et al. 2004). Taking advantage of the VLT/MUSE observations of the Mrk 463 system, we can then produce a $A_{H\alpha}$ map. Following the prescription of Lee et al. (2009), we assume case B recombination with an intrinsic $H\alpha/H\beta$ ratio of 2.86, a Milky Way extinction curve, and $R_V = 3.1$ such that $A_{H\alpha}$ is given by:

$$A_{H\alpha} = 5.91 \log \left(\frac{f_{H\alpha}}{f_{H\beta}} \right) - 2.70,$$

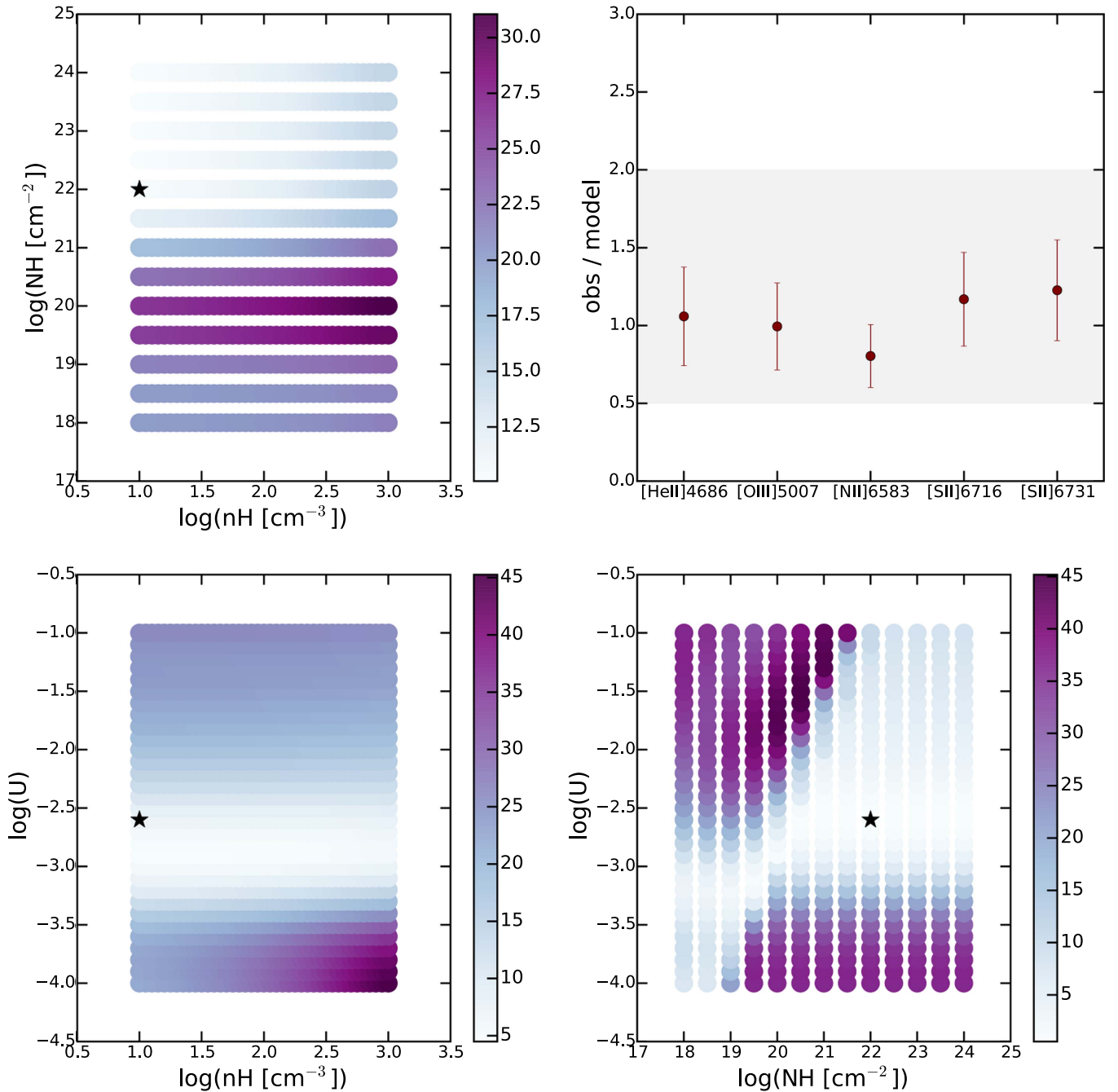


Figure 19. Results of the CLOUDY simulation for a representative point inside the southern emission line region. The top left panel shows the resulting column density, N_{H} , as a function of the volume density, n_{H} . The top right panel presents the ratio of observed to modeled flux for the best-fitting set of parameters and the corresponding error bars. The bottom-left panel shows the values of reduced χ^2 for the $\log U$ and $\log n_{\text{H}}$ combinations, while the bottom-right panel presents the relation for $\log U$ and $\log N_{\text{H}}$. The color scheme in all panels represents the reduced χ^2 , while the star shows the location of the best-fitting (minimum reduced χ^2) solution.

where $f_{\text{H}\alpha}$ and $f_{\text{H}\beta}$ are the total emission line fluxes on the $\text{H}\alpha$ and $\text{H}\beta$ lines derived following the procedure described in Section 3.1. The resulting map is shown in Figure 18. As can be seen, most of the system is only affected by relatively low extinction levels, $A_{\text{H}\alpha} < 1$. However, there are specific areas that appear subject to higher optical obscuration. These include some of the regions where we previously identified high levels of star formation to the east of the Mrk 463E nucleus, and the area between the two nuclei, where we can see values of $A_{\text{H}\alpha} \sim 1.5$ –2. While locally important, these relatively modest obscuration levels do not significantly affect our conclusions

about the morphologies and kinematics derived from the optical VLT/MUSE IFU maps presented here, and they are even less important for the near-IR analysis shown in Section 3.2.

5.2. Energetics of the Emission Line Region

As described in Section 3.1, we identify an emission line region to the south of the system, consistent with AGN powering. This region closely resembles the “Hanny’s Voorwerp” structure associated with IC 2497 (Lintott et al. 2009), which was found serendipitously by visual

inspection of the galaxy optical images carried out as part of the Galaxy Zoo project (Lintott et al. 2008). Hanny’s Voorwerp appears to be ionized by the nearby AGN in IC 2497, which must have been at least 100 times more luminous $\sim 100,000$ years earlier (Schawinski et al. 2010; Keel et al. 2012b; Sartori et al. 2016). For Mrk 463, the southern region is ~ 11 kpc away from the Mrk 463E nucleus, which corresponds to $\sim 40,000$ light years. Based on the evident alignment between this emission line region and the ionization cone arising from the Mrk 463E core, we can safely neglect the contribution from the Mrk 463W AGN. In turn, we can estimate the luminosity necessary to supply the ionizing flux required to explain the observed spectrum of the southern region.

In order to carry out this computation, we selected a region in the center of the emission region enclosing most of its flux. For constraints, we used the observed luminosities and their errors in the $H\alpha$, $H\beta$, $[\text{He II}] 4686 \text{ \AA}$, $[\text{O III}] 5007 \text{ \AA}$, $[\text{N II}] 6583 \text{ \AA}$, $[\text{S II}] 6717 \text{ \AA}$ and $[\text{S II}] 6731 \text{ \AA}$ lines, all measured from the VLT/MUSE optical IFU observations. We then performed radiative transfer simulations using the plasma ionization code CLOUDY version 13.04 (Ferland et al. 2013). We considered two different cases: (1) a matter-bounded scenario in which the main parameters are U , the dimensionless ionization parameter, n_{H} , the hydrogen volume density, and N_{H} , the hydrogen column density; and (2) a radiation-bounded case, whose only parameters are U and n_{H} . In both cases, we assumed that the input AGN spectrum was given by a broken power law of the form $L_{\nu} \propto \nu^{\alpha}$, with $\alpha = -0.5$ for $E < 13.6 \text{ eV}$, $\alpha = -1.5$ in the range $13.6 < E < 0.5 \text{ keV}$, and $\alpha = -0.8$ at $E > 0.5 \text{ keV}$, consistent with the observed spectrum of local AGN (e.g., Elvis et al. 1994; Kraemer et al. 2009).

For each resolution element in the southern emission region, we used the grid of simulations carried out using CLOUDY in order to find the best fit to the intrinsic emission line ratios, all computed with respect to the $H\beta$ line. From this solution, we can obtain the corresponding value of Q , the number of ionizing photons emitted per unit of time, which is defined by

$$U = \frac{Q(H)}{4\pi r_0^2 n(H)c}, \quad (1)$$

where r_0 is the distance between the AGN and the cloud. We then use this value to obtain the corresponding intrinsic bolometric luminosity by assuming an intrinsic AGN spectral shape, such as the one given by, e.g., Elvis et al. (1994). The results of the simulations are presented in Figure 19. The best-fitting value for $\log U$ can be found between -2.9 and -2.6 , with a mean value of -2.7 .

As can be seen in Figure 19, the resulting fits are not very sensitive to the value of n_{H} . Indeed, models with the same U and N_{H} but different values of n_{H} yield very similar reduced χ^2 . This is critical in our calculation, as the required intrinsic AGN bolometric luminosity is proportional to $U \times n_{\text{H}}$, as can be seen in Equation (1). For the n_{H} calculation, we assume a fully-ionized gas, as was done for the Voorwerpjes (Keel et al. 2012a). Hence, the atomic hydrogen column density is the same as the electron density, $n_{\text{H}} = n_e$, which can be estimated from the ratio of the two $[\text{S II}]$ lines. Furthermore, we can neglect the contribution from molecular hydrogen, given that no molecular gas was detected at the position of the southern ionized cloud. From the observed values of the $[\text{S II}]$

6716/6731 ratio, we estimate an allowed average n_{H} range in the southern emission region of $10\text{--}100 \text{ atoms cm}^{-3}$. In turn, this implies bolometric AGN luminosities in the range of $2.7 \times 10^{45} \text{ erg s}^{-1}$ to $1.8 \times 10^{46} \text{ erg s}^{-1}$. We compare this value with the current AGN luminosity, as observed in X-rays. From *Chandra* observations, Bianchi et al. (2008) reported a 2–10 keV luminosity of $1.5 \times 10^{43} \text{ erg s}^{-1}$. Using their reported N_{H} value of $7.1 \times 10^{23} \text{ atoms cm}^{-2}$, we can estimate an intrinsic 2–10 keV luminosity of $9.9 \times 10^{43} \text{ erg s}^{-1}$. Assuming a bolometric correction from 2–10 keV of 10 (e.g., Marconi et al. 2004), this implies that the intrinsic AGN luminosity was a factor of $\sim 3\text{--}20$ times higher $\sim 40,000$ years ago, when the light that photo-ionized the southern region was emitted. This is similar to the sample of Hanny’s Voorwerp-like objects studied by Keel et al. (2017).

Short-term (up to decades) AGN variability by factors of ~ 5 has been observed in the hard X-ray luminosity before (e.g., Ulrich et al. 1997, and references therein). Hence, our results imply that the AGN activity in Mrk 463E could have changed by up to an order of magnitude for the last $\sim 40,000$. This is consistent with so-called “standard” variability, and thus consistent with the AGN lifetime of $\sim 100,000$ years suggested by Schawinski et al. (2015).

5.3. Feeding the SMBHs

The *Chandra* X-ray data show that the SMBH in the Mrk 463E nucleus is accreting at a $\sim 5\times$ higher rate, and is more obscured than the one in Mrk 463W. In turn, most of the larger-scale structures detected by the VLT/MUSE observations, in both continuum and emission lines, appear to be associated preferentially with the Mrk 463E nucleus. Similarly, both the southern emission line region and the outflowing cloud in the north appear to be well-aligned with the apparent biconical gradient, which in turn is also linked to the Mrk 463E AGN. This could be interpreted as the AGN in Mrk 463E being older and more evolved than the one in Mrk 463W, which is then most likely just starting its activity. Additional evidence pointing in that direction was presented in the previous section, where a lifetime greater than 40,000 years was estimated for the Mrk 463E AGN.

Based on the ALMA $^{12}\text{CO}(2\text{--}1)$ observations presented in Section 3.3, we see that both nuclei contain significant molecular gas reservoirs, $\sim 10^9 M_{\odot}$ around Mrk 463E and $\sim 5 \times 10^8 M_{\odot}$ surrounding Mrk 463W. We further find $\sim 3 \times 10^7 M_{\odot}$ in molecular gas in clouds in between the two nuclei. This amount of material, albeit small, could be readily available to feed both SMBHs in the near future. Indeed, as presented in Section 4.3, we estimate that the gas infalling rate onto the Mrk 463E nucleus is over three orders of magnitude larger than the SMBH accretion rate inferred from the X-ray luminosity. Hence, we can conclude that both nuclei have the potential fuel to feed quasar-like luminosity systems and increase their SMBH masses significantly, by adding $> 10^8 M_{\odot}$. However, as presented in Section 4.1, the outflow rate of the ionized gas is similar to the infall rate of the molecular gas onto the central regions of the system. Therefore, while the accretion rate onto the SMBHs is relatively small, there appears to be a rough balance between the material infalling (as molecular gas) and outflowing (as ionized gas). This outflowing material does not, however, appear to affect the star formation processes, as it is highly anisotropic and not aligned with the stellar disks.

5.4. Possible Evolution

Currently, the two nuclei in Mrk 463 are both active, perhaps at a relatively low level, heavily obscured at $N_{\text{H}} \sim 10^{23}$ atoms cm^{-2} and separated by ~ 4 kpc. As the merger continues, it is expected that the two nuclei will get closer over timescales of 10^8 years. The molecular gas that is now surrounding each nucleus will likely tend to concentrate such that a fraction of it will likely be available for accretion onto the SMBHs, while at the same time increasing the nuclear obscuration. Depending on the exact (and as-yet unknown) dynamics of the nuclei, the system may pass through a stage analogous to that which the nearby dual AGN NGC6240 is experiencing now, in which both nuclei are separated by ~ 1 kpc and are heavily obscured (Komossa et al. 2003), while most of the gas is concentrated between the two nuclei (Tacconi et al. 1999; Iono et al. 2007; G. Privon et al. 2018, in preparation). Alternatively, the gas could remain concentrated on each nucleus as they approach each other, thus creating a configuration similar to what it is observed now in the central region of Arp 220 (e.g., Manohar & Scoville 2017, and references therein). While the amount of ongoing SMBH accretion in Arp 220 is still uncertain (e.g., Barcos-Muñoz et al. 2015), *Chandra* (Iwasawa et al. 2005) and NuSTAR observations (Teng et al. 2015) suggest that there is at least one heavily obscured, Compton-thick AGN associated with the system, on the western nucleus. In any case, following the scenario suggested by Treister et al. (2010), we can expect that, after $\sim 1\text{--}2 \times 10^8$ years, the collapsed nuclear region will start to become unobscured due to the effects of radiation pressure, thus revealing an unobscured quasar, perhaps similar to the one observed in Mrk 231, with strong ionized winds and ultrafast outflows (Feruglio et al. 2015), like those already observed in this system, associated with the Mrk 463E nucleus.

We note that the case of Mrk 463 highlights the difficulty of using the instantaneous AGN luminosity to place objects within evolutionary sequences. At least one nucleus shows evidence for changing luminosities on timescales of $10^{4\text{--}5}$ years, which is significantly shorter than those expected for dynamical evolution of the system (e.g., LaMassa et al. 2015; Parker et al. 2016; Gezari et al. 2017). This suggests it is likely problematic to use AGN luminosity as even a broad indicator of evolutionary stage, because one or both nuclei can rapidly rise or drop in luminosity at any point. This further highlights the need for multi-wavelength spatially-resolved spectroscopy over large spatial scales, as presented here, in order to fully understand the evolutionary stage of these complex merging galaxies.

6. Conclusions

We have presented optical and near-IR seeing-limited IFU data for the nearby dual AGN Mrk 463, complemented by relatively high-resolution band 6 ALMA data covering both the $^{12}\text{CO}(2\text{--}1)$ transition and the surrounding ~ 220 GHz continuum. The multiwavelength spatially resolved spectroscopy reveals a very complex system, in which the gas morphology is highly distorted due to both the ongoing major merger and the SMBH accretion activity. Optical emission lines, such as [O III] and $\text{H}\beta$, reveal the presence of AGN-ionized emission line regions extending beyond 10 kpc away from the nuclear regions, while the $\text{H}\alpha$ and $\text{Pa}\alpha$ emission lines trace star-forming regions up to even larger distances. The He II 4686 line traces the influence of the AGN in both the nuclei and the

extended regions. In general, we find relatively low optical extinction in this system, $A_{\text{H}\alpha} < 1$, although moderate values are found toward specific isolated regions. Kinematically, the [O III] and $\text{H}\beta$ maps show evidence for a clear biconical outflow in the central region of the Mrk 463E galaxy, in which we infer mass outflow rates of $\sim 512 M_{\odot} \text{s}^{-1}$. We further detected an outflowing region at $>600 \text{ km s}^{-1}$, about 15 kpc to the north of the Mrk 463E nucleus. Velocity gradients in these emission lines could also be detected in the tidal tails, most likely associated with the dynamics of the galaxy merger. From an energetics analysis of the southern emission line region—which, according to the observed line ratios, is consistent with being photoionized by the AGN emission—we conclude that the AGN luminosity, and thus SMBH accretion rate, on the Mrk 463E nucleus changed by a factor 3–20 in the last 40,000 years, much like the handful of known Hanny’s Voorwerp-like objects. The structure of the stellar kinematics reveals the presence of a strong velocity gradient to the west of the Mrk 463W nucleus. While this gradient can be fitted by a Keplerian disk, it can also be associated to the tidal plumes originating from the ongoing major merger, thus suggesting that the system is undergoing a second or later close pass of the nuclei. Indeed, the rather smooth optical continuum spatial profile of that region, as well as the spatial separation of $\sim 3\text{--}4$ kpc between the presumed stellar disk and the Mrk 463W nucleus, strongly supports the latter interpretation.

From the ALMA data, we can see significant molecular gas reservoirs, $\sim 10^9 M_{\odot}$ in Mrk 463E and $\sim 5 \times 10^8 M_{\odot}$ on the western nucleus, surrounding each nuclei, closer than ~ 1 kpc but not directly on the AGN locations. The molecular gas around each nuclei presents significant velocity gradients, thus suggesting a ring-like structure. While it is expected that a significant fraction of this molecular gas should be available for the SMBH to accrete, by comparing the molecular gas directly overlapping with the AGN to the accretion rate inferred from the AGN luminosity, we conclude that only a very small fraction, $<0.01\%$, of the surrounding material is actively feeding the SMBH. Considering the observed properties of the gas in this system, we conclude that, in this system, molecular gas is infalling onto the central regions at a rate of $\sim 100s M_{\odot} \text{yr}^{-1}$. Of this, a relatively small fraction, $\sim 0.0017 M_{\odot} \text{yr}^{-1}$, is accreted onto the SMBH. This small amount of accreted material is able to generate an outflow of ionized gas that pushes $\sim 500 M_{\odot} \text{yr}^{-1}$ away from the nucleus. Hence, we can consider this major galaxy merger like a machine that receives large amounts of molecular gas and in return expels that material in the form of collimated ionized winds, being fueled by only a very small fraction, 10^{-5} , of that material being accreted by the SMBH.

We can speculate that, in the future, as the two nuclei get closer to each other, the surrounding molecular gas will concentrate on the coalescent nucleus, increasing both the SMBH accretion and nuclear obscuration. After ~ 100 million years, the radiation pressure should be strong enough to evaporate most of the surrounding material, revealing an unobscured, high-luminosity AGN, i.e., quasars, characterized by strong winds and outflows like those already observed in nearby galaxies such as Mrk 231. High-resolution dynamical modeling of this system would allow us to better predict the future of gas-rich major galaxy mergers.

While these multiwavelength observations have been critical to increase our understanding of the gas in the dual AGN

Mrk 463, it is clear that higher-resolution data are necessary in order to understand, for example, the behavior of the gas actively feeding the SMBHs now and its connection to the merger dynamics. It is possible now to obtain these data thanks to the long baseline, >10 km, modes available with ALMA, which would yield spatial resolutions of tens of parsecs for the molecular gas observations. Similarly, observations of higher-J CO transitions would allow to measure physical parameters, such as temperature, and to study the denser material, which might be located closer to the SMBHs.

We thank the anonymous referee for a very positive and constructive report that helped improve this paper. We acknowledge support from: CONICYT-Chile grants Basal-CATA PFB-06/2007 (F.E.B., E.T., C.R.), FONDECYT Regular 1141218 (F.E.B., C.R.), and 1160999 (E.T.), FONDECYT Postdoctorado 3150361 (G.C.P.), EMBIGGEN Anillo ACT1101 (F.E.B., E.T., G.C.P., C.R.); the Ministry of Economy, Development, and Tourism's Millennium Science Initiative through grant IC120009, awarded to The Millennium Institute of Astrophysics, MAS (F.E.B.); Swiss National Science Foundation Grants PPO0P2 138979 and PPO0P2 166159 (K.S., L.S.), and the China-CONICYT fund (CR). V. U. acknowledges funding support from the University of California Chancellor's Postdoctoral Fellowship. This paper makes use of the following ALMA data: ADS/JAO.ALMA#2013.1.00525.S. ALMA is a partnership of ESO (representing its member states), NSF (USA), and NINS (Japan), together with NRC (Canada), NSC and ASIAA (Taiwan), and KASI (Republic of Korea), in cooperation with the Republic of Chile. The Joint ALMA Observatory is operated by ESO, AUI/NRAO, and NAOJ. The National Radio Astronomy Observatory is a facility of the National Science Foundation operated under cooperative agreement by Associated Universities, Inc. This work is partly sponsored by the Chinese Academy of Sciences (CAS), through a grant to the CAS South America Center for Astronomy (CASSACA) in Santiago, Chile.

Facilities: VLT: Yepun (MUSE and SINFONI), ALMA, CXO.

Software: Fluxer, IRAF, CLOUDY, IDL, CASA, FUS, numpy, matplotlib, pyspeckit.

ORCID iDs

Ezequiel Treister  <https://orcid.org/0000-0001-7568-6412>
 George C. Privon  <https://orcid.org/0000-0003-3474-1125>
 Franz E. Bauer  <https://orcid.org/0000-0002-8686-8737>
 Kevin Schawinski  <https://orcid.org/0000-0001-5464-0888>
 Hugo Messias  <https://orcid.org/0000-0002-2985-7994>
 Claudio Ricci  <https://orcid.org/0000-0001-5231-2645>
 Vivian U  <https://orcid.org/0000-0002-1912-0024>
 Caitlin Casey  <https://orcid.org/0000-0002-0930-6466>
 Michael Koss  <https://orcid.org/0000-0002-7998-9581>
 David B. Sanders  <https://orcid.org/0000-0002-1233-9998>
 C. Megan Urry  <https://orcid.org/0000-0002-0745-9792>

References

Adams, T. F. 1977, *ApJS*, **33**, 19
 Alatalo, K., Lacy, M., Lanz, L., et al. 2015, *ApJ*, **798**, 31

- Alloin, D., Barvainis, R., Gordon, M. A., & Antonucci, R. R. J. 1992, *A&A*, **265**, 429
 Bacon, R., Accardo, M., Adjali, L., et al. 2010, *Proc. SPIE*, **7735**, 773508
 Baldwin, J. A., Phillips, M. M., & Terlevich, R. 1981, *PASP*, **93**, 5
 Bär, R., Weigel, A. K., Sartori, L. F., et al. 2017, *MNRAS*, **466**, 2879
 Barcos-Muñoz, L., Leroy, A. K., Evans, A. S., et al. 2015, *ApJ*, **799**, 10
 Barnes, J. E., & Hernquist, L. E. 1991, *ApJL*, **370**, L65
 Bekki, K., & Shioya, Y. 2000, *A&A*, **362**, 97
 Benson, A. J., Bower, R. G., Frenk, C. S., et al. 2003, *ApJ*, **599**, 38
 Bertola, F., Cappellari, M., Funes, J. G., et al. 1998, *ApJL*, **509**, L93
 Bianchi, S., Chiaberge, M., Piconcelli, E., Guainazzi, M., & Matt, G. 2008, *MNRAS*, **386**, 105
 Blecha, L., Loeb, A., & Narayan, R. 2013, *MNRAS*, **429**, 2594
 Bolatto, A. D., Wolfire, M., & Leroy, A. K. 2013, *ARA&A*, **51**, 207
 Briggs, D. S. 1995, *BAAS*, **27**, 1444
 Brusa, M., Bongiorno, A., Cresci, G., et al. 2015, *MNRAS*, **446**, 2394
 Caplan, J., & Deharveng, L. 1986, *A&A*, **155**, 297
 Cappellari, M. 2017, *MNRAS*, **466**, 798
 Cappellari, M., & Copin, Y. 2003, *MNRAS*, **342**, 345
 Cappellari, M., & Emsellem, E. 2004, *PASP*, **116**, 138
 Chatzichristou, E. T., & Vanderriest, C. 1995, *A&A*, **298**, 343
 Croton, D. J., Springel, V., White, S. D. M., et al. 2006, *MNRAS*, **365**, 11
 Di Matteo, T., Colberg, J., Springel, V., Hernquist, L., & Sijacki, D. 2008, *ApJ*, **676**, 33
 Di Matteo, T., Springel, V., & Hernquist, L. 2005, *Natur*, **433**, 604
 Eisenhauer, F., Abuter, R., Bickert, K., et al. 2003, *Proc. SPIE*, **4841**, 1548
 Elvis, M., Wilkes, B. J., McDowell, J. C., et al. 1994, *ApJS*, **95**, 1
 Evans, A. S., Mazzarella, J. M., Surace, J. A., & Sanders, D. B. 2002, *ApJ*, **580**, 749
 Falco, E. E., Kurtz, M. J., Geller, M. J., et al. 1999, *PASP*, **111**, 438
 Falcón-Barroso, J., Sánchez-Blázquez, P., Vazdekis, A., et al. 2011, *A&A*, **532**, A95
 Farrah, D., Bernard-Salas, J., Spoon, H. W. W., et al. 2007, *ApJ*, **667**, 149
 Ferland, G. J., Porter, R. L., van Hoof, P. A. M., et al. 2013, *RMxAA*, **49**, 137
 Feruglio, C., Fiore, F., Carniani, S., et al. 2015, *A&A*, **583**, A99
 Freudling, W., Romaniello, M., Bramich, D. M., et al. 2013, *A&A*, **559**, A96
 Fu, H., Myers, A. D., Djorgovski, S. G., & Yan, L. 2011a, *ApJ*, **733**, 103
 Fu, H., Zhang, Z.-Y., Assef, R. J., et al. 2011b, *ApJL*, **740**, L44
 García-Burillo, S., Combes, F., Usero, A., et al. 2014, *A&A*, **567**, A125
 Gezari, S., Hung, T., Cenko, S. B., et al. 2017, *ApJ*, **835**, 144
 Ginsburg, A., & Mirocha, J. 2011, PySpecKit: Python Spectroscopic Toolkit, Astrophysics Source Code Library, ascl:1109.001
 González-López, J., Bauer, F. E., Romero-Cañizales, C., et al. 2017, *A&A*, **597**, A41
 Hibbard, J. E., & van Gorkom, J. H. 1996, *AJ*, **111**, 655
 Hinshaw, G., Weiland, J. L., Hill, R. S., et al. 2009, *ApJS*, **180**, 225
 Hopkins, P. F., Hernquist, L., Cox, T. J., et al. 2006, *ApJS*, **163**, 1
 Hopkins, P. F., Hernquist, L., Martini, P., et al. 2005, *ApJL*, **625**, L71
 Hutchings, J. B., & Neff, S. G. 1989, *AJ*, **97**, 1306
 Iono, D., Wilson, C. D., Takakuwa, S., et al. 2007, *ApJ*, **659**, 283
 Iwasawa, K., Sanders, D. B., Evans, A. S., et al. 2005, *MNRAS*, **357**, 565
 Kauffmann, G., & Charlot, S. 1998, *MNRAS*, **297**, L23
 Kauffmann, G., Heckman, T. M., Tremonti, C., et al. 2003, *MNRAS*, **346**, 1055
 Keel, W. C., Chojnowski, S. D., Bennert, V. N., et al. 2012a, *MNRAS*, **420**, 878
 Keel, W. C., Lintott, C. J., Maksym, W. P., et al. 2017, *ApJ*, **835**, 256
 Keel, W. C., Lintott, C. J., Schawinski, K., et al. 2012b, *AJ*, **144**, 66
 Kewley, L. J., Dopita, M. A., Sutherland, R. S., Heisler, C. A., & Trevena, J. 2001, *ApJ*, **556**, 121
 Kewley, L. J., Groves, B., Kauffmann, G., & Heckman, T. 2006, *MNRAS*, **372**, 961
 Komossa, S., Burwitz, V., Hasinger, G., et al. 2003, *ApJL*, **582**, L15
 Koss, M., Mushotzky, R., Treister, E., et al. 2011, *ApJL*, **735**, L42
 Koss, M., Mushotzky, R., Treister, E., et al. 2012, *ApJL*, **746**, L22
 Kraemer, S. B., Trippe, M. L., Crenshaw, D. M., et al. 2009, *ApJ*, **698**, 106
 LaMassa, S. M., Cales, S., Moran, E. C., et al. 2015, *ApJ*, **800**, 144
 Lee, J. C., Gil de Paz, A., Tremonti, C., et al. 2009, *ApJ*, **706**, 599
 Lintott, C. J., Schawinski, K., Keel, W., et al. 2009, *MNRAS*, **399**, 129
 Lintott, C. J., Schawinski, K., Slosar, A., et al. 2008, *MNRAS*, **389**, 1179
 Liu, X., Shen, Y., Strauss, M. A., & Hao, L. 2011, *ApJ*, **737**, 101
 Maíz-Apellániz, J., Pérez, E., & Mas-Hesse, J. M. 2004, *AJ*, **128**, 1196
 Manohar, S., & Scoville, N. 2017, *ApJ*, **835**, 127
 Marconi, A., Risaliti, G., Gilli, R., et al. 2004, *MNRAS*, **351**, 169

- Mazzarella, J. M., Iwasawa, K., Vavilkin, T., et al. 2012, *AJ*, 144, 125
- Mazzarella, J. M., Soifer, B. T., Graham, J. R., et al. 1991, *AJ*, 102, 1241
- McGurk, R. C., Max, C. E., Medling, A. M., Shields, G. A., & Comerford, J. M. 2015, *ApJ*, 811, 14
- Mihos, J. C., & Hernquist, L. 1996, *ApJ*, 464, 641
- Modigliani, A., Hummel, W., Abuter, R., et al. 2007, arXiv:astro-ph/0701297
- Müller Sánchez, F., Davies, R. I., Genzel, R., et al. 2009, *ApJ*, 691, 749
- Müller-Sánchez, F., Comerford, J., Stern, D., & Harrison, F. A. 2016, *ApJ*, 830, 50
- Müller-Sánchez, F., Prieto, M. A., Hicks, E. K. S., et al. 2011, *ApJ*, 739, 69
- Nevin, R., Comerford, J. M., Müller-Sánchez, F., Barrows, R., & Cooper, M. C. 2018, *MNRAS*, 473, 2160
- Oliva, E. 1997, in ASP Conf. Ser. 113, IAU Coll. 159: Emission Lines in Active Galaxies: New Methods and Techniques, ed. B. M. Peterson, F.-Z. Cheng, & A. S. Wilson (San Francisco, CA: ASP), 288
- Osterbrock, D. E., & Ferland, G. J. 2006, *Astrophysics of Gaseous Nebulae and Active Galactic Nuclei* (2nd ed.; Sausalito, CA: University Science Books)
- Parker, M. L., Komossa, S., Kollatschny, W., et al. 2016, *MNRAS*, 461, 1927
- Petrosian, A. R., Saakian, K. A., & Khachikian, E. E. 1978, *Afz*, 14, 69
- Ricci, C., Bauer, F. E., Treister, E., et al. 2017, *MNRAS*, 468, 1273
- Rich, J. A., Kewley, L. J., & Dopita, M. A. 2011, *ApJ*, 734, 87
- Rich, J. A., Kewley, L. J., & Dopita, M. A. 2015, *ApJS*, 221, 28
- Rieke, G. H., Blaylock, M., Decin, L., et al. 2008, *AJ*, 135, 2245
- Rupke, D. S. N., & Veilleux, S. 2011, *ApJL*, 729, L27
- Sanders, D. B., & Mirabel, I. F. 1996, *ARA&A*, 34, 749
- Sanders, D. B., Soifer, B. T., Elias, J. H., et al. 1988, *ApJ*, 325, 74
- Sartori, L. F., Schawinski, K., Koss, M., et al. 2016, *MNRAS*, 457, 3629
- Sartori, L. F., Schawinski, K., Treister, E., et al. 2015, *MNRAS*, 454, 3722
- Schawinski, K., Evans, D. A., Virani, S., et al. 2010, *ApJL*, 724, L30
- Schawinski, K., Koss, M., Berney, S., & Sartori, L. F. 2015, *MNRAS*, 451, 2517
- Schawinski, K., Thomas, D., Sarzi, M., et al. 2007, *MNRAS*, 382, 1415
- Schawinski, K., Khochfar, S., Kaviraj, S., et al. 2006, *Natur*, 442, 888
- Scoville, N., Murchikova, L., Walter, F., et al. 2017, *ApJ*, 836, 66
- Shen, Y., Liu, X., Greene, J. E., & Strauss, M. A. 2011, *ApJ*, 735, 48
- Shirazi, M., & Brinchmann, J. 2012, *MNRAS*, 421, 1043
- Soifer, B. T., Rowan-Robinson, M., Houck, J. R., et al. 1984, *ApJL*, 278, L71
- Solomon, P. M., & Vanden Bout, P. A. 2005, *ARA&A*, 43, 677
- Springel, V., Di Matteo, T., & Hernquist, L. 2005, *MNRAS*, 361, 776
- Storchi-Bergmann, T., Lopes, R. D. S., McGregor, P. J., et al. 2010, *MNRAS*, 402, 819
- Tacconi, L. J., Genzel, R., Tecza, M., et al. 1999, *ApJ*, 524, 732
- Teng, S. H., Rigby, J. R., Stern, D., et al. 2015, *ApJ*, 814, 56
- Treister, E., Natarajan, P., Sanders, D. B., et al. 2010, *Sci*, 328, 600
- Treister, E., Schawinski, K., Urry, C. M., & Simmons, B. D. 2012, *ApJL*, 758, L39
- Trentham, N., Kormendy, J., & Sanders, D. B. 1999, *AJ*, 117, 2152
- Ulrich, M.-H., Maraschi, L., & Urry, C. M. 1997, *ARA&A*, 35, 445
- Van Wassenhove, S., Volonteri, M., Mayer, L., et al. 2012, *ApJL*, 748, L7
- Veilleux, S., Cecil, G., & Bland-Hawthorn, J. 2005, *ARA&A*, 43, 769
- Veilleux, S., Meléndez, M., Sturm, E., et al. 2013, *ApJ*, 776, 27
- Veilleux, S., & Osterbrock, D. E. 1987, *ApJS*, 63, 295
- Volonteri, M., Haardt, F., & Madau, P. 2003, *ApJ*, 582, 559
- Weilbacher, P. M., Streicher, O., Urrutia, T., et al. 2014, in ASP Conf. Ser. 485, *Astronomical Data Analysis Software and Systems XXIII*, ed. N. Manset & P. Forshay (San Francisco, CA: ASP), 451